Corrosion protection in a coating defect on AA2024-T3 by lithium carbonate inhibitor leaching

An experimentally validated FEM approach

Abdelrahman, N.; Van den Steen, N.; Özkan, C.; Visser, P.; Lamaka, S. V.; Böttcher, R.; Mol, J. M.C.; Terryn, H.; Hauffman, T.; More Authors

DOI
10.1016/j.corsci.2025.112861

Publication date
2025

Document Version
Final published version

Published in
Corrosion Science

Corrosion Science 250 (2025) 112861

Contents lists available at ScienceDirect

Corrosion Science

journal homepage: www.elsevier.com/locate/corsci

Corrosion protection in a coating defect on AA2024-T3 by lithium carbonate inhibitor leaching: An experimentally validated FEM approach

N. Abdelrahman [a,*], N. Van den Steen [a], C. Özkan [b], C. Wang [c,d], C. Song [c], P. Visser [e], S.V. Lamaka [c], S. Kallip [c,f], R. Böttcher [g], J.M.C. Mol [b], M.L. Zheludkevich [c,h], H. Terryn [a,b], T. Hauffman [a], M. Meeusen [a]

[a] Research group Sustainable Materials Engineering (SUME), lab of Electrochemical and Surface Engineering (SURF), Vrije Universiteit Brussel, Pleinlaan 2, 1050 Brussel, Belgium
[b] Department of Materials Science and Engineering, Corrosion Technology and Electrochemistry group, Delft University of Technology, Mekelweg 2, 2628 CD Delft, The Netherlands
[c] Institute of Surface Science, Helmholtz-Zentrum Hereon, 21502 Geesthacht, Germany
[d] School of Materials Science and Engineering, Southeast University, 211189, Nanjing, China
[e] AkzoNobel, Rijksstraatweg 31, 2171 AJ, Sassenheim, The Netherlands
[f] Institute of Chemistry, University of Tartu, Ravila 14a, 50411 Tartu, Estonia
[g] Airbus Central R&T, Willy-Messerschmitt-Straße 1, 82024 Taufkirchen, Germany
[h] Institute of Materials Science, Faculty of Engineering, Kiel University, 24143 Kiel, Germany

ARTICLE INFO

Keywords:
FEM
Lithium carbonate
Corrosion protection
COMSOL multiphysics

ABSTRACT

A 2D finite element model is developed to simulate the protection of active protective coatings in a defect. The leaching kinetics, inhibitor-electrolyte reactions and electrochemical surface reactions on homogenized AA2024-T3, are considered. Changes in local oxygen distribution, pH, and current density over time are validated using surface scanning micro-probe techniques. The limitations posed by the prediction of surface current density at the metal interface using a FEM model with a homogenized microstructure are identified and addressed. The validated FEM is then used to predict inhibitor concentration and pH dependent on the initial inhibitor pigment concentration in an organic coating.

1. Introduction

For years, the aerospace industry has relied on hexavalent chromium as the main corrosion inhibitor to protect aluminum alloys from corrosion [1]. However, its toxicity and carcinogenic nature have made it subject to strict international environmental, health and safety legislation [2]. Consequently, the worldwide search for alternative corrosion inhibitor technologies is intense, with the aid of both experimental and modeling efforts. Introducing a potential substitute in practice necessitates comprehensive mechanistic understanding and testing across various environments and exposure durations [3,4].

Lithium carbonate is suggested as a potential candidate as it provides corrosion protection through the initial formation of intermediate phases of hydrated aluminum oxide (pseudoboehmite (PB)) and later through a created layered double hydroxide (LDH) layer on the surface of aluminum alloys as lithium ions increase in concentration [5,6]. Ongoing studies are addressing crucial aspects of the coating matrix, aiming to enable the rapid release of lithium carbonate providing early protection while still guaranteeing ongoing release and corrosion protection during long term exposure [7]. Investigations of the influence of pH on pigment release and surface protection have indicated a requirement for a slightly alkaline environment, attributed to the initial step of LDH formation involving the dissolution of the oxide layer and the release of aluminum ions [8]. Other studies have explored LDH formation using varying concentrations of different lithium compounds [9]. However, determining the optimal lithium-leaching pigment, its concentration and the overall coating formulation necessitates further experimental and modeling efforts.

Finite element modeling (FEM) tools have proven to be valuable in supporting experimental endeavors, functioning as both a design and testing toolkit. The increasing sophistication of modeling platforms and their capacity to incorporate additional processes without overwhelming computational resources highlight their growing importance. In the corrosion and corrosion protection research domain, FEM has successfully provided predictions validated through experimental data.

* Corresponding author.
E-mail address: Nourhan.abdelrahman@vub.be (N. Abdelrahman).

https://doi.org/10.1016/j.corsci.2025.112861
Received 5 December 2024; Received in revised form 15 February 2025; Accepted 9 March 2025
Available online 18 March 2025

Prior work, Guseva et al. [10], utilized a combined experimental and modeling approach to identify the existing corrosion species resulting from the dissolution of an aluminum surface and the change in the concentration of each species depending on pH values. Accordingly, they were able to introduce the most significant hydrolysis and homogeneous reactions as well as an estimation of their reaction kinetics into a model of aluminum pitting corrosion. This work gave essential information on which species are considered to be essential when building further models of AA2024-T3. Abodi et al. [11] introduced the different phases of aluminum alloy 2024 as a heterogeneous surface into a model where the cathodic and anodic activity were varying depending on each phase's elemental composition. The model then presented the areas where pit formation could be expected. The heterogeneity of AA2024-T3 surface and how it could be represented into numerical models motivated more research where the benefits included utilizing experimental measurements on heterogeneous surfaces to validate the results of homogeneous models, as well as, establishing the models' capabilities to extend their structures from homogeneous to a heterogeneous alloy. Based on experimentally observes inhomogeneous dissolution pattern of sacrificial anode coating, Dolgikh et al. [12] introduced the concept of "active node" to model corrosion protection of steel cut-edge by hot-dop galvanized Al (Zn, Mg) coatings. Following successful implementation of that, Snihirova et al. [13] modeled the effect of pitting in a galvanic couple between AA2024 and Ti-based alloy Ti6AlV4 through implementing an active node. A node with length of 70 μm is implemented on AA2024 surface with the rate constant of the electrode reactions 10 times higher than its value in the remaining surface. The results supported the capability of this approach to show the effect of an active pit on the pH distribution within the electrolyte.

FEM has been extended to include corrosion protection processes as well. Corrosion protection with magnesium-loaded organic coatings was investigated, considering electrode reactions, electrolyte interactions, and species precipitation on AA2024-T3 surface [14]. While validated successfully, this model lacked consideration of the leaching effects of inhibiting pigments within a coating.

Several studies employed FEM to explore the effects related to the properties of organic coatings and corrosion inhibitor particles [15,16]. Focus was placed on modeling and tailoring inhibitor release, seeing this as a direct means of determining inhibitor levels in the electrolyte and, consequently, the protection level at different time points. In a study utilizing cerium-loaded coatings, the model's qualitative validation over time through optical measurements is noted [16]. However, model transferability and extension to other inhibitors would not be possible as it is dependent on a combined approach of experimental and model calculation.

The aim of the present work is to introduce a toolbox to be used for the prediction of lithium carbonate corrosion protection level provided at varying initial status of the system, including primer — defect — aluminum — electrolyte. The toolbox also holds the possibility of being extended and used for other inhibitor pigments. To this aim, a FEM model is used to predict the corrosion protection in a coating defect containing active protective species. Interfaces between the electrolyte and the atmosphere, the coating and the electrolyte and the metal surface and the electrolyte are included. Changes in the distribution and concentration of different species are affected by the different domains definitions, and this is reflected in the chemical reactions included in the model. Corrosion protection provided by lithium carbonate is included, as well as its effect on the surface current density. Model inputs are introduced from two sets of experimental data: potentiodynamic polarization (PDP) and inhibitor leaching measurements. Model results represent the changes in all species concentration over time, as well as change in surface current density. Model calculation of oxygen concentration, pH and current density are validated using measurements of surface scanning micro-probe techniques.

2. Experimental

A schematic graph representing the paper's inputs, outputs, and flow is presented in Fig. 1. The input parameters are extracted through the processing of two experimental sets of measurements: lithium carbonate leaching measurements and potentiodynamic polarization (PDP). The inhibitor leaching fitting is done in COMSOL to obtain the governing parameters of Li^+ production and concentration in the electrolyte. PDP measurements fitting is done in PIRODE software [17] to obtain the effect of Li^+ on corrosion levels. In this work, the leaching fitting results are directly implemented in the corrosion protection model. The processed inputs were utilized to describe the onset of corrosion, the dissociation of the pigment, the diffusion of the ions throughout all model domains (primer, topcoat, and electrolyte) and the protection effect of the inhibitor on the AA2024-T3 surface. The results of the model were validated against SECM measurements of pH and O_2 as well as SVET measurements of electrolyte current density.

2.1. Materials and samples preparation

Potentiodynamic polarization measurements were conducted with 2 mm thick AA2024-T3 sheets cut into 20 mm × 20 mm samples. Samples are sanded with waterproof SiC sandpapers under running water with progressively finer grit sizes of 320, 800, 1200, 2000 and 4000. After sanding, the samples were polished with fine diamond suspensions with particle sizes of 3 and 1 μm. After polishing, the samples were cleaned in an ultrasonic bath with isopropanol for 15 min and then dried using compressed air, resulting in a mirror-like finish.

Polymer coated samples of anodized, unsanded AA2024-T3 were used to measure the release of lithium from the primer coating, which is composed as described in [18]. Panels were cut into samples with a surface area of 28 cm^2. A scalpel was used to introduce 20 straight cuts with 5 cm length and 50 μm width each penetrating through the coating and extending to the metal surface. The same coated sheets were utilized for the scanning electrochemical microscopy (SECM) in potentiometric mode for pH measurements and in amperometric mode for measuring local concentration of dissolved oxygen and scanning vibrating electrode technique (SVET) for logging local current densities. Additionally, a separate sheet was coated with primer matrix previously stated [18] but devoid of any inhibitor particles and topped with a layer of topcoat 43 μm thick as reference. Both sheets were then cut into samples of 15 mm by 17.5 mm. A machine-made U-shaped scribe with a depth of 200 μm, relative to the top of the coating, was introduced into the coating layer to expose the metal surface to produce the samples seen in Fig. 2 where a Keyence profilometer VR-5000 was used to visualize the geometry of the scribe with optical magnification of ×40 (resolution 7.4 μm in X and Y and in 0.1 μm in Z direction).

2.2. Analysis techniques

2.2.1. Potentiodynamic polarization (PDP)

Polished samples are exposed to 250 ml electrolyte with varying inhibitor concentrations in a conventional three electrode electrochemical cell setup. Lithium carbonate concentrations of 0.1 mM, 1 mM, 5 mM and 10 mM were used in addition to the 0.1 *M* NaCl electrolyte to record multiple PDP analyzing the change of corrosion protection level in bulk conditions related to the change in inhibitor concentration. A platinum counter electrode and a reference electrode of saturated Ag/AgCl were used. A reference solution of 0.1 *M* NaCl electrolyte was used to record the non-inhibiting case on bare AA2024-T3 samples. The scan rate was set as 0.1 mV s^{-1}, to be scanned across ±250 mV versus OCP. Starting the scan at the cathodic side and shifting towards the anodic, scans were recorded with multiple repetitions ranging from 3 to 5.

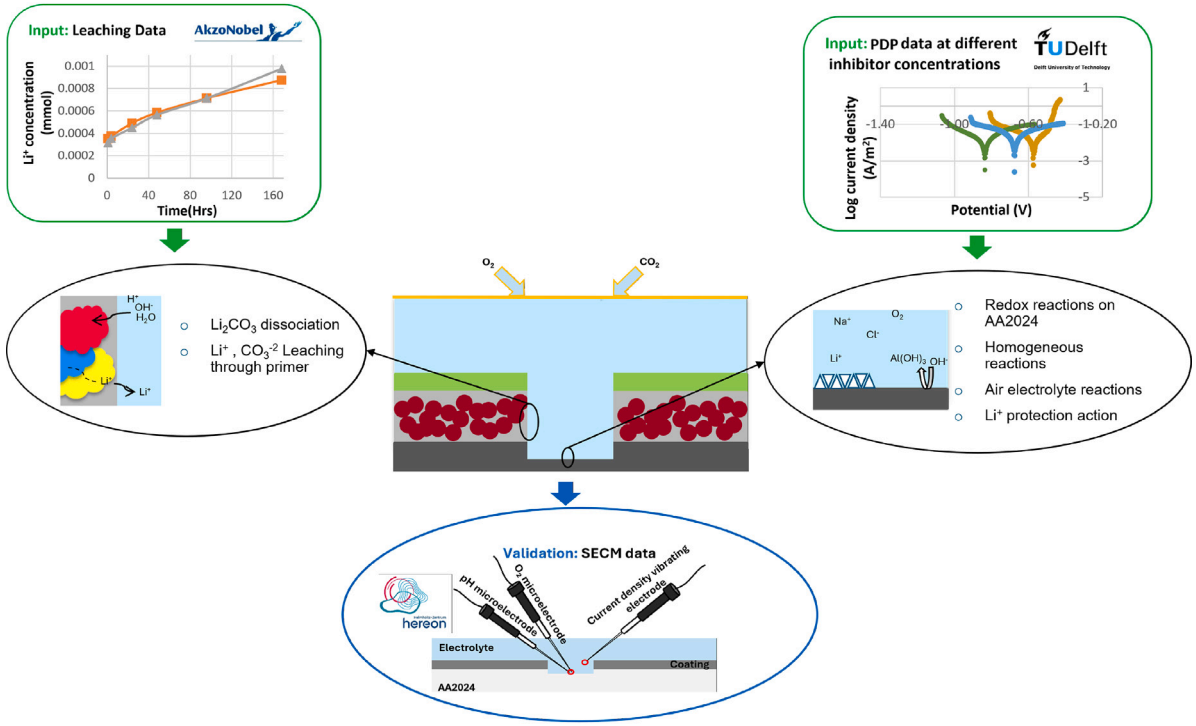

Fig. 1. Model overview including inputs, approach, and validation. Inputs are potentiodynamic polarization measurements (upper right) and leaching measurements (upper left). Model's geometry and approach are summarized in the center of the graph. Validation through local electrochemical micro-probe measurements at the bottom.

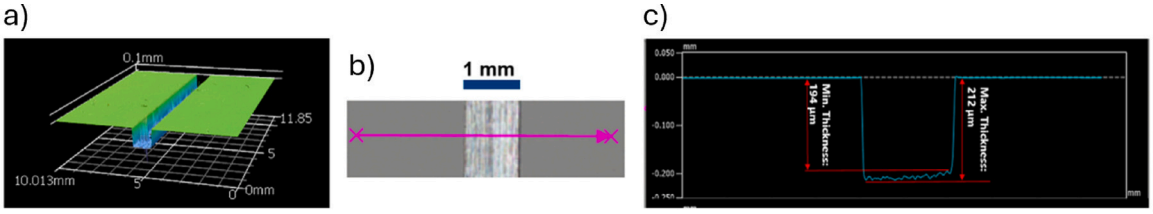

Fig. 2. Scribe in the middle, reaching to the alloy substrate. The scribe is of 200 µ depth and 1000 µm width, through the coating to the bare alloy. (a) Profilometric map; (b) optical photo top view and (c) cross-section profile of a coated sample with the scribe.

2.2.2. Local electrochemical probe techniques (SECM & SVET)

The distribution of local concentration of dissolved oxygen, local pH and local current density were measured by Clark type amperometric micro-probe, pH-sensitive micro-probe with the tip made of pH sensitive glass and insulated Pt-Ir micro-probe correspondingly. These three parameters were measured either simultaneously (O_2 and pH) on a selected limited area of the exposed scribe defect or consecutively (local current density) in the scribe and above the coating around the scribe, following the topography of the defect in the coating. Dissolved oxygen (DO) sensitive amperometric micro-probe with a tip diameter of 25 µm (OX-25 Unisense, Denmark) and pH micro-probe with a tip diameter of 10 µm (pH-10 Unisense, Denmark) were connected to a fx-6 UniAmp (Unisense, Denmark). Both micro-probes were calibrated considering the salinity and temperature of the solution. The analog output from fx-6 UniAmp was integrated into a commercial SVET-SIET system from Applicable Electronics™, controlled by LV4 software from Sciencewares™. This allowed synchronizing the position of each micro-probe with the corresponding signal.

Fig. 3 shows the schematic of the sample with 0.1 *M* NaCl as the electrolyte with a volume of 2.5 mL to 1 µL and thickness of 3 mm to 30 µm; the photograph of the electrochemical cell for local current density measurements, using SVET, optical micrographs of pH & O_2 micro-probes positioned in the scribe, schematic of the two micro-probes positioned at 20 µm from the surface and one micro-probe positioned at 200 µm and the cycles representing the changes in electrolyte height throughout the measurements time.

Surface scans were performed on samples coated with lithium carbonate loaded primer, as well as, samples coated with only the primer as uninhibited reference. The micro-probes monitoring oxygen concentration and pH were positioned at 20 µm from the metal surface and recorded the changes across the surface from the moment of adding the electrolyte up to 6 to 8 h of immersion. While the measurements start with a water layer thickness of 0.5 mm in the uninhibited reference case and 3 mm in the lithium carbonate protected case, the water layer thickness decreased over time due to evaporation and was refilled in order to be restored to the initial thickness.

Additionally, custom-made experimental prototype of SVET equipment ("LocalProber" provided by University of Tartu and Tehnolabor OÜ, Estonia) was used to record the current density vectors in separate x, y and z components in the electrolyte above the defect. An insulated Pt-Ir micro-probe (Microprobes Inc., USA) with a 10–20 µm spherical platinum black tip was used. The micro-probe was held at an offset of 200 µm from the surface and then followed the surface topography as it scanned over the entire exposed defect area of the sample. The probe vibrated with an amplitude of 15 µm and with the frequency of 76.2 Hz, and local ionic current density values were mapped. It should be noted that differently from SECM, SVET measurements took place over the

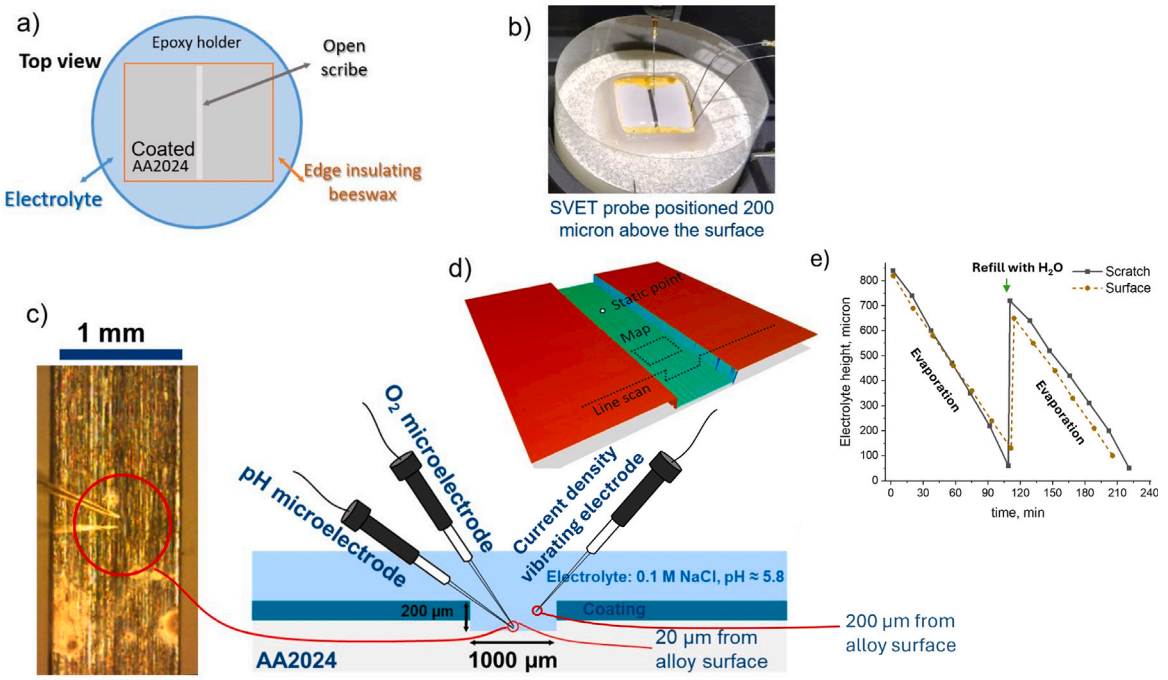

Fig. 3. Experimental setup for surface scanning micro-probe measurements. (a) Schematic of the sample in the cell and corresponding optical photo in (b) showing the vibrating micro-probe for SVET measurements with reference and ground electrodes. (c) Optical micrograph showing a top view of the scribe area with the pH and O_2 micro-probes position in the scribe illustrated into a schematic of the pH and O2 micro-probe position in the scribe, cross-section view. (d) Experimental scanning modes employed: "static point" measurements in time, horizontal "map" inside the scribe and horizontal line scan across coated sample including lowering the micro-probes 200 µm inside the scribe. (e) The evaporation and refiling cycle through which the electrolyte underwent during the surface measurements.

whole electrolyte exposed defect area, which should allow estimating localized zone distribution (cathodic, anodic) on the sample.

As the local probe measurements described are utilized for FEM validation, It is important to note that investigations regarding the stirring effect of the vibrating microprobes were conducted in previous studies [19–21] with the conclusion stating that the effect occurs locally in the region below the probe. However, this effect vanishes within minutes, making any changes insignificant in the long run.

2.3. Finite Element Model(FEM)

A 2D finite element model is built in COMSOL Multiphysics version 5.4, a commercially available FEM software, using the tertiary current distribution (tcd) module. This module studies the evolution of chemical species transported by diffusion and migration, assuming they are dilute and that the mixture properties correspond to those of the solvent. The chemical species transport is solved for through the mass conservation equation. In addition, a chemical node was implemented to include the evolution of species through the added chemical reactions.

The geometry used in the model is displayed in Fig. 4. The dimensions of the geometry are chosen to replicate those of the conducted leaching experiments, and then later adjusted to resemble the conducted SECM/SVET validation measurements to ensure validation accuracy. The leaching fitting geometry includes a defect with a width of 100 µm with no depth, a primer thickness of 23.6 µm, topcoat thickness of 43 µm and a water layer height of 1.78 cm. The uninhibited reference case had the same primer and topcoat thickness but with an aqueous solution height of 500 µm, defect width and depth of 1 mm and 134 ± to 8 µm, respectively. The second scenario with the lithium carbonate loaded coating maintains similar dimensions to the first, but features a water layer height of 3 mm. It should be noted here that the evaporation effects observed in the measurements were not applied to the model, so the water layer thickness remained the same throughout the solution time. Simulation times were up to 168 h for the leaching fitting model. Solution time points of 6 and 11 h were extracted for model validation.

A 1D finite element model is built in PIRODE, a commercial software for the study of electrochemical reactions on rotating electrodes. It allows for the incorporation of electrolyte reactions, and encompasses the transport of species towards and away from the electrode through diffusion, migration, and convection.

2.3.1. Approach and governing equations

While the topcoat as seen in Fig. 4 and the primer covers the surface of AA2024-T3 alloy, the topcoat hinders water molecules from traveling to the primer or the metal surface. This means the alloy surface, underneath the primer-topcoat areas, is protected from any corrosive effects. In case of coating defects, the AA2024-T3 surface is no longer protected through the barrier effect, and redox reactions will occur at the alloy surface producing aluminum cations. Reactions begin to take place within the electrolyte layer among the electrolyte ionic species, the aluminum cation and the dissolved gas species. Water uptake into the primer matrix from the scratch area causes the coating system to swell. Upon arrival of water molecules at the pigment particles, they begin to dissolve, leaving behind a space ultimately filled with aqueous solution. With time, intra-primer pathways for diffusion of aqueous electrolytes enable more inhibitor particles to dissolve. This process results in the formation of interconnected water channels in the primer, allowing dissolution of particles further away from the defect-primer interface [18]. Dissolved species in the primer would diffuse through the formed interconnected channels towards the scribe where they will interact with AA2024-T3 and electrolyte species, resulting in the formation of complex and protective Li-intercalated LDH. This layer is able to provide corrosion protection to the surface. It should be emphasized that the model does not include the LDH formation but rather the corrosion protection effect of the layer.

The model introduces the changes occurring over time in the exposed coating-substrate system: topcoat and primer, and electrolyte layer on top of an aluminum surface. The change in concentration

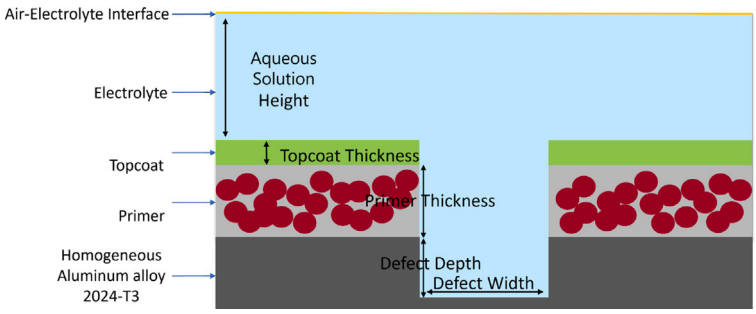

Fig. 4. Description of domains and dimension parameters of the implemented geometry in COMSOL resembling the prepared experimental sample.

Table 1
Species included in the model with their charge, diffusion coefficient in the electrolyte D_e and their initial concentration.

Species	Charge	D_e [m^2 s^{-1}]	Initial Conc [mol/m^3]	Reference
Na^+	+1	$1.33 \cdot 10^{-09}$	100	[11]
Cl^-	−1	$2.03 \cdot 10^{-09}$	100	[11]
Al^{3+}	+3	$5.41 \cdot 10^{-10}$	$4.47 \cdot 10^{-13}$	[11]
$AlOH^{2+}$	+2	$5.41 \cdot 10^{-10}$	$4.47 \cdot 10^{-11}$	[11]
$Al(OH)_2^+$	+1	$5.41 \cdot 10^{-10}$	$4.47 \cdot 10^{-09}$	[11]
$Al(OH)_3$	0	$5.41 \cdot 10^{-10}$	$9.94 \cdot 10^{-07}$	[11]
$AlCl^{2+}$	+2	$5.41 \cdot 10^{-10}$	$6.72 \cdot 10^{-13}$	[11]
$AlClOH^+$	+1	$5.41 \cdot 10^{-10}$	$7.12 \cdot 10^{-11}$	[11]
O_2	0	$1.98 \cdot 10^{-09}$	$2.58 \cdot 10^{-01}$	[11]
Li_2CO_3	0	10^{-16}	0, 3026	[22]
Li^+	+1	$1.03 \cdot 10^{-09}$	0	[22]
CO_3^{2-}	−2	$0.955 \cdot 10^{-09}$	0	[23]
H_2O	0	$2.3 \cdot 10^{-09}$	55 300	[11]
OH^-	−1	$5.2 \cdot 10^{-09}$	$9.99 \cdot 10^{-05}$	[11]
H^+	+1	$9.3 \cdot 10^{-09}$	$9.99 \cdot 10^{-05}$	[11]
CO_2	0	$2 \cdot 10^{-09}$	0.014	[23]
HCO_3^-	−1	$1.1 \cdot 10^{-09}$	0	[22]
H_2CO_3	0	10^{-09}	0	[22]

across the different domains from primer, topcoat and water layer are represented through the mass conservation equation the concentration changes of species k over time can be represented as:

$$\frac{\partial c_k}{\partial t} = -\vec{\nabla}\vec{N}_k + R_k \tag{1}$$

where $\frac{\partial c_k}{\partial t}$ represents the change in the concentration of species k over time. The change is due to either the movement of the species which is represented by the flux term $\vec{N}_k$ or due to the chemical reactions occurring represented by the term R_k. Initially, the concentration of different species is the same in all domains. An exception is made for the lithium carbonate particles, which are only present in the primer throughout the process.

The flux could be divided into the processes of diffusion and migration using Nernst–Planck equation (convection term is neglected as no stirring is expected):

$$\vec{N}_k = -D_k\vec{\nabla}c_k - z_k u_k F c_k \vec{\nabla}\vec{U} \tag{2}$$

with D_k is the diffusion coefficient of species k, z_k is the species charge, u_K is the mobility, F is Faraday constant and $\vec{\nabla}\vec{U}$ is the potential gradient.

The homogeneous reactions term represents the overall rate by which a reaction proceeds and is represented as :

$$R_k = k_f c_f - k_b c_p \tag{3}$$

where k_f and k_b are respectively the forward and backward reaction rate constants. c_f and c_b are the concentrations of the reactants and products included in the chemical reaction.

Corrosion of aluminum in an electrolyte rich with oxygen occurring at the electrode surface of the substrate-electrolyte interface is implemented through the usage of boundary conditions at this surface. The implemented boundary equation is concentration dependent Butler-Volmer equation:

$$i_{loc} = i_0(C_R \cdot exp\left(\frac{\alpha_a F}{RT}\eta\right) - C_O \cdot exp\left(\frac{-\alpha_c F}{RT}\right)\eta) \tag{4}$$

where i_{loc} is the local current density due to either the cathodic or the anodic branch of the reactions as the model implements one equation per each half of the redox reaction, i_0 is the exchange current density, C_R, C_O are the concentration of the reduced and oxidized species respectively, α_a, α_c are the anodic and cathodic charge transfer coefficients, η is the over-potential and R and T are the universal gas constant and the temperature. This equation represents one half of the corrosion process. In order to implement both halves, two reaction blocks are added to the model with charge conservation consideration included, so the total current density of the surface has to be zero as expressed in Eq. (5):

$$|i_{loc_{an}}| = |i_{loc_{cath}}| \tag{5}$$

An insulation boundary condition (Eq. (6)) is imposed at all other walls of the geometry as production of current away from the electrode surface is excluded:

$$i = 0 \tag{6}$$

A no-flux boundary condition is added to all walls except the air-electrolyte interface through Eq. (7). This is to indicate that there is no species transport in or out of the model domain. The air-electrolyte boundary is excluded as a constant concentration of CO_2 and O_2 is imposed to represent the dissolution of these gases into the electrolyte. Introducing such a boundary guarantees that the effect of electrolyte layer on oxygen diffusion is taken into consideration in the model as the layer thickness controls the rate of oxygen replenishment near the electrode. Consequently, the effect of oxygen diffusion limited current density is implemented in the model.

$$N_k = 0 \tag{7}$$

2.3.2. Model parameters and assumptions

Two model cases are explained in this work, the first is an uninhibited reference case with a coating that does not contain any inhibitor pigments. The second is built with the same definition and parameters of the first case, but with the addition of Li_2CO_3 inhibitor particles in the primer and their follow-up protection process. Multiple assumptions were made in the building of the two cases, including:

- The microstructural heterogeneity of AA2024-T3 is not included, i.e. the behavior of the individual intermetallic (IM) is not taken into account. The surface of AA2024-T3 is homogenized by taking the EC information from the PDP measurements to originate from the entire alloy homogeneously, with no local spots for cathodic or anodic processes. This is done to remove the need of considering pit initiation and directing the focus towards the

Table 2
Reactions considered in the model and their forward and backward reaction rates.

Reaction	Equilibrium constant (K)	k_f	k_b	Reference
$H_2O \rightleftharpoons H^+ + OH^-$		1.5	$8.302 \cdot 10^{12}$	[11]
$Al^{3+} + H_2O \rightleftharpoons AlOH^{2+} + H^+$		$4.2 \cdot 10^{04}$	$4.4 \cdot 10^{06}$	[11]
$AlOH^{2+} + H_2O \rightleftharpoons Al(OH)_2^+ + H^+$		$4.2 \cdot 10^{04}$	$3.6 \cdot 10^{06}$	[11]
$Al(OH)_2^+ + H_2O \rightleftharpoons Al(OH)_3 + H^+$		$5.58 \cdot 10^{04}$	$2.8 \cdot 10^{06}$	[11]
$Al^{3+} + Cl^- \rightleftharpoons AlCl^{2+}$		$2.26 \cdot 10^{-1}$	$1.36 \cdot 10^{-03}$	[11]
$AlOH^{2+} + Cl^- \rightleftharpoons AlOHCl^+$		19	$1.03 \cdot 10^{-01}$	[11]
$Li_2CO_3 \rightleftharpoons 2Li^+ + CO_3^-$	$8.15 \cdot 10^{-04}$	$6.6 \cdot 10^{-04}$	0.0809	[22]
$CO_2 + H_2O \rightleftharpoons H_2CO_3$	848	0.03	25.44	[22,23]
$H_2CO_3 \rightleftharpoons HCO_3^- + H^+$	$4.4 \cdot 10^{-07}$	$5 \cdot 10^{-04}$	1118.64	[23]
$HCO_3^- \rightleftharpoons CO_3^{2-} + H^+$	$4.6 \cdot 10^{-11}$	10^{-04}	$2.13 \cdot 10^6$	[23]

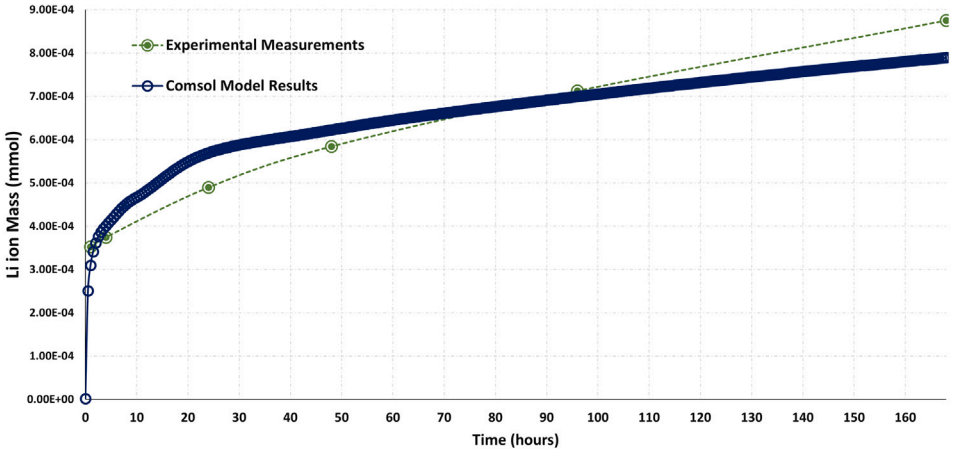

Fig. 5. The results of FEM leaching fitting versus the leaching measurements in terms of the number of moles of Li^+ found in the electrolyte.

broad corrosion protection scheme. However, the heterogeneous effect will be considered in a later step for the purposes of current density calculation.

- The anodization layer on top of the alloy surface is not included in the model, as well as any follow-up effect or change it could cause. This is done as the defect cuts through the anodization layer as well. In addition, no undercoating corrosion or delamination process is taken into account.
- As aluminum forms the majority element of AA2024 [24], the model ignores redox reactions of any other alloying elements in AA2024-T3. The oxidation and reduction occurring at the metal surface taken into account in the model are limited to aluminum oxidation and oxygen reduction only. This is represented by Eqs. (8), (9), respectively.

$$Al \rightleftharpoons Al^{3+} + 3e^- \tag{8}$$

$$O_2 + 2H_2O + 4e^- \rightleftharpoons 4OH^- \tag{9}$$

- Considering the low concentrations of different species in the electrolyte, the individual diffusion constants of involved species are taken to be similar to the diffusion coefficient in pure water. The diffusion coefficient in primer is obtained from fitting the model so that the leached lithium-ion in the electrolyte resemble the results of the leaching measurements as shown in Fig. 5. The fitting step took into consideration that diffusion of species in both the primer and the topcoat are slower than in the electrolyte [25]. It is understood that the diffusion coefficient values are dependent on the pore size of the diffusive medium [26]. For the system under study, pore sizes vary with the dissolution of inhibitor pigments in the primer. Consequently, an averaged diffusion coefficient was assigned for each species within the primer, calculated as 10% of the respective diffusion coefficient in water. Since the topcoat serves as a barrier, the diffusion coefficient in the topcoat are 10% of the respective values in the primer. The model includes 17 species in the electrolyte and primer. All species and their related parameters are introduced in Table 1 while Table 2 shows the reactions included in the model between the previously mentioned species.
- Table 2 shows the reactions included in the model between the species defined in Table 1. It includes the implemented reaction rate constants values of k_f and k_b where they represent the forward and backward reaction rates, respectively, where they are related to the reaction equilibrium constant K through:

$$K = \frac{k_f}{k_b} \tag{10}$$

- The water layer thickness on the AA2024-T3 surface is assumed to remain constant throughout the simulation time. While this assumption ignores a significant factor with a high probability of varying, the simplicity introduced by assuming a constant water layer thickness serves to establish a validated base model. This fundamental model can subsequently be refined and elevated to a more sophisticated level by incorporating variations in the electrolyte layer, accounting for the small but potentially impactful changes over time.
- The model assumes a uniform distribution of the lithium carbonate pigment throughout the primer. This allows for the estimation of pigment behavior in an averaged format, eliminating the complications associated with the specific location and distribution of individual pigment particles. By opting for this uniform distribution approach, the model achieves a level of abstraction that facilitates a clearer understanding of the average behavior of the lithium carbonate pigment within the primer.

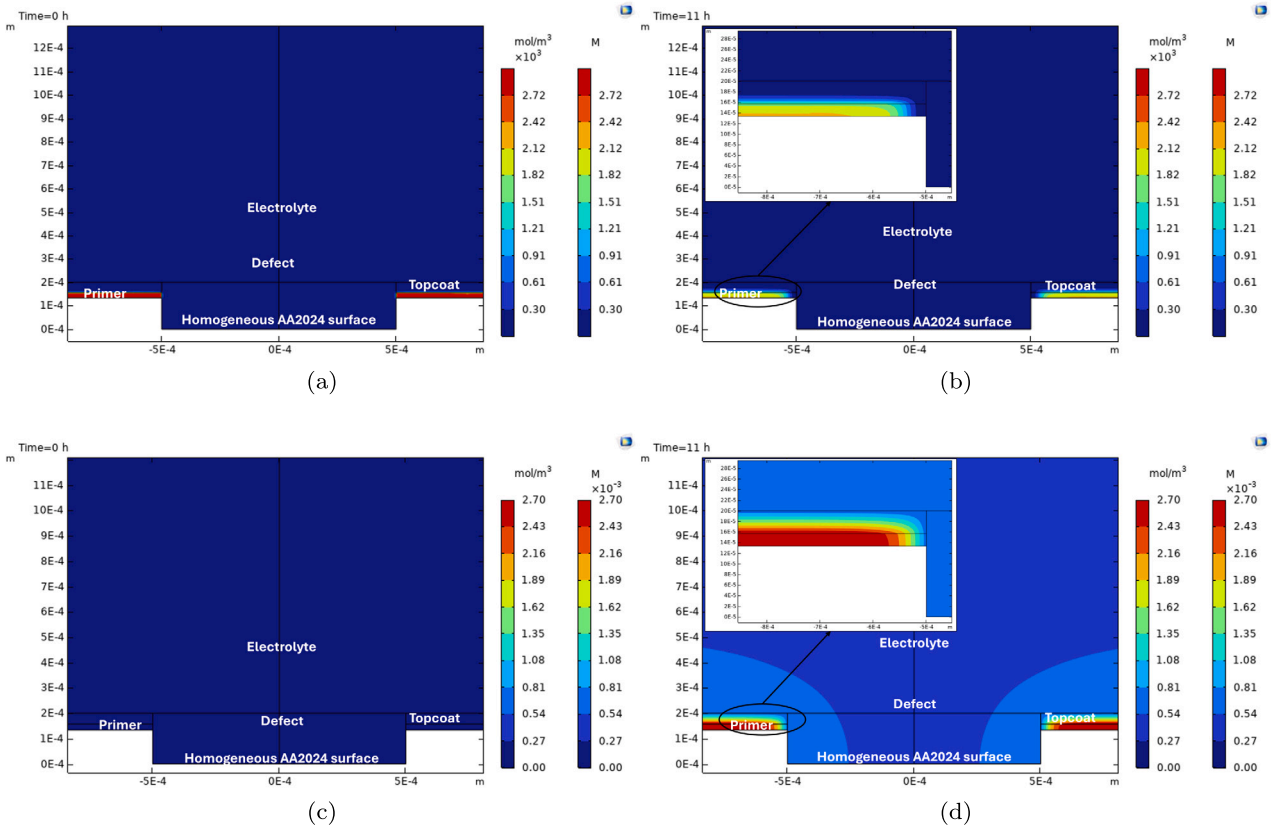

Fig. 6. Predicted model concentrations of Li_2CO_3 and Li^+ in the coating and defect over time. (a) Concentration of Li_2CO_3 at 0 h, (b) concentration of Li_2CO_3 at 11 h, (c) concentration of Li^+ at 0 h, (d) concentration of Li^+ at 11 h.

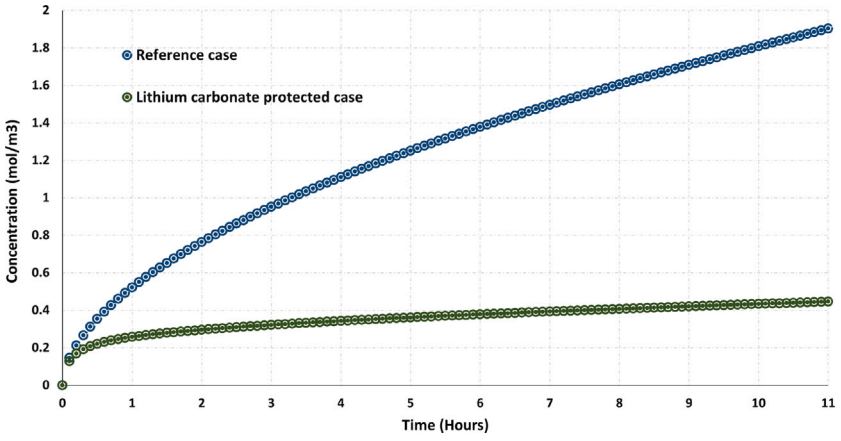

Fig. 7. Comparison between uninhibited reference and system containing corrosion inhibitor model results: evolution of the average concentration of sum of all species containing aluminum ions in defect area over 11 h.

3. Results & Discussion

3.1. PDP results & fitting

Figure 22 in supplementary Information contains all the conducted PDP measurements, with Table 3 listing the fitted kinetic values for the different iterations. It should be noted that the fitting utilized the linear region around OCP of the measurements, ignoring the further areas containing a limited current density. Following the change in open circuit potential (OCP) values as lithium carbonate concentration increases, it is observed that initially a shift towards less negative potentials at 0.1 mM and 1 mM concentrations of lithium carbonate compared to the case of only 0.1 *M* sodium chloride. The shift is caused by a decrease in anodic current density, indicating the inhibition of the anodic branch and a decrease of corrosion rate. At higher concentration of lithium carbonate, 5 mM and 10 mM, a more negative potential associated with a higher anodic current density with a certain suppression of the cathodic currents are observed. This could be attributed to high pH values (>10.6) [27,28] which may cause a faster rate of attack on the aluminum oxide layer relative to the formation rate of the intermediate inhibition molecules and the LDH layer which damps the inhibition level [6]. The fitted kinetics in Table 3 for all replicas are averaged, which are then implemented in COMSOL model using a linear interpolation function to establish a relationship between the concentration of Li_2CO_3 in the solution and the corrosion susceptibility or protection level of the alloy surface.

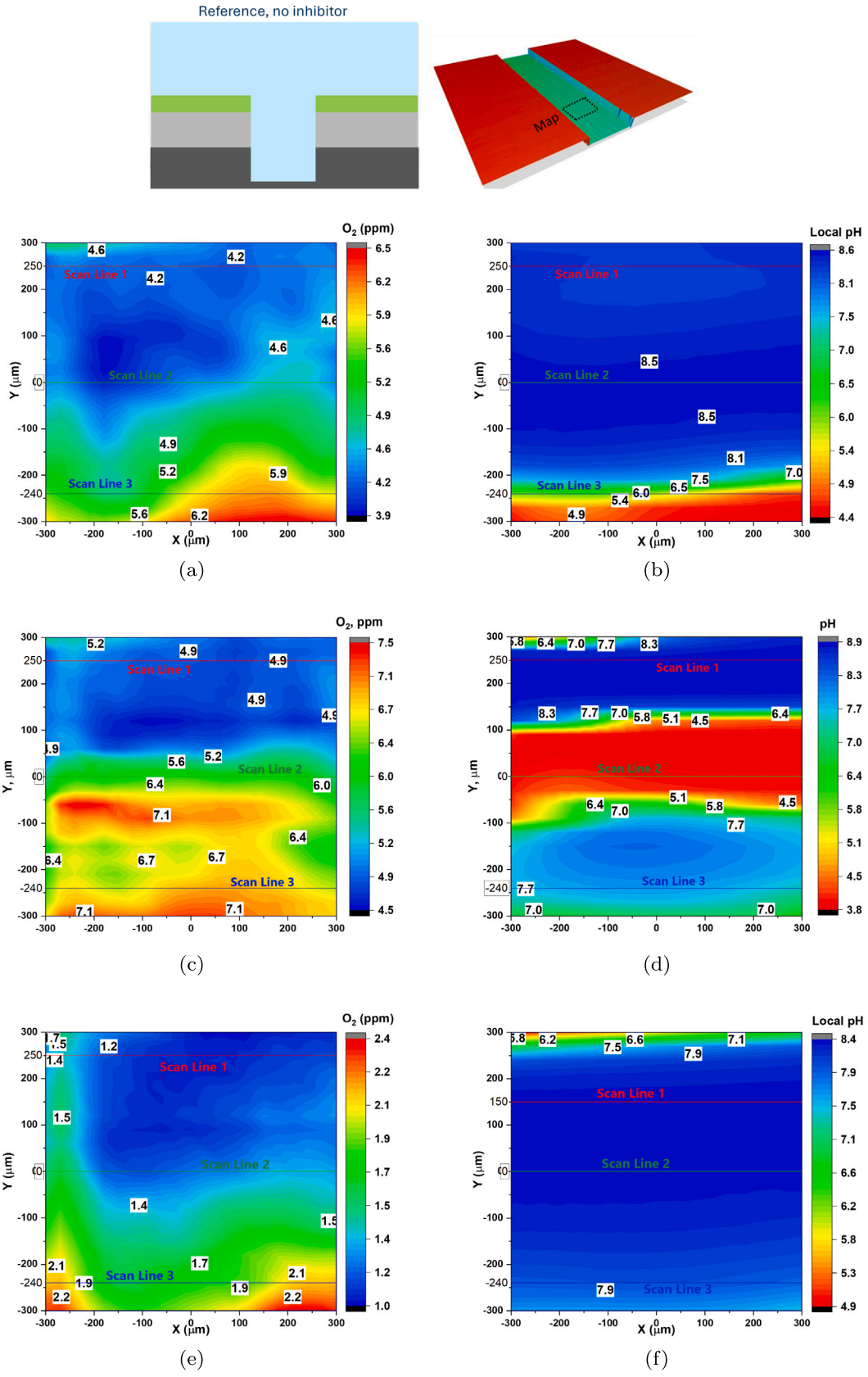

Fig. 8. SECM of uninhibited reference sample: Top view of pH and O_2 concentration surface scans in the coating defect on AA2024-T3 after 1, 1.5 h, and 4 h. (a) Oxygen concentration at 1 h, (b) pH at 1 h, (c) oxygen concentration at 1.5 h, (d) pH at 1.5 h, (e) oxygen concentration at 4 h, (f) pH at 4 h.

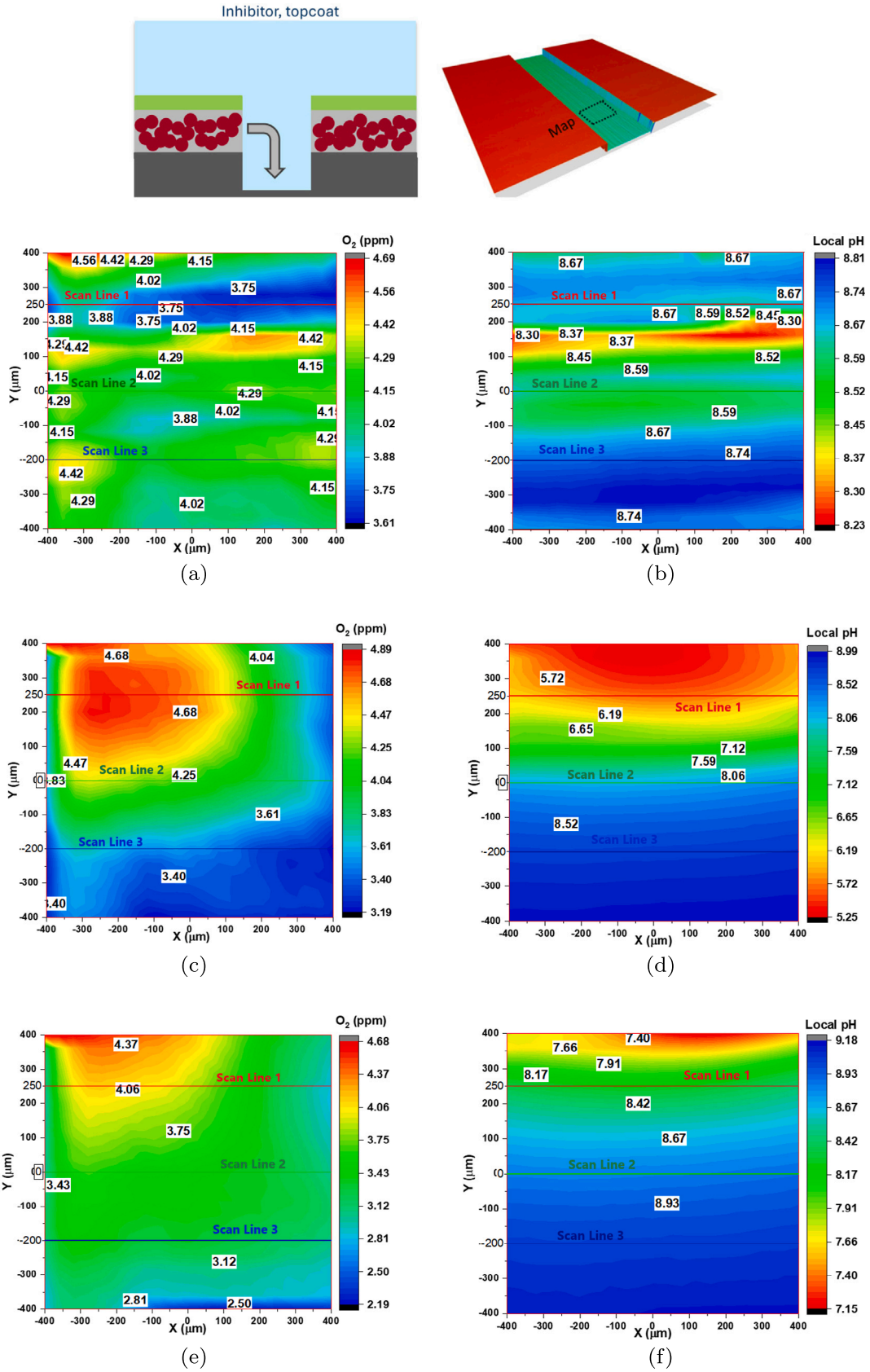

Fig. 9. SECM of lithium carbonate corrosion inhibitor sample: Top view of pH and O_2 concentration surface scans in the coating defect on AA2024-T3 after 30 min, 3 h and 6 h. (a) Oxygen concentration at 30 min, (b) pH at 30 min, (c) oxygen concentration at 3 h, (d) pH at 3 h, (e) oxygen concentration at 6 h, (f) pH at 6 h.

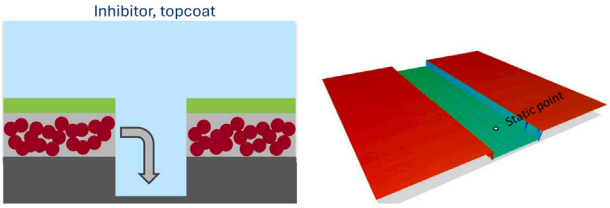

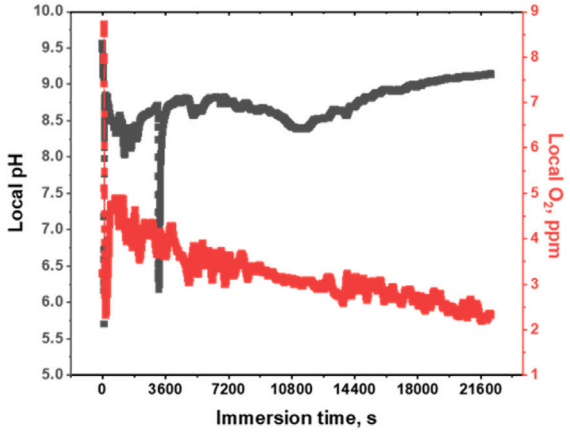

(a)

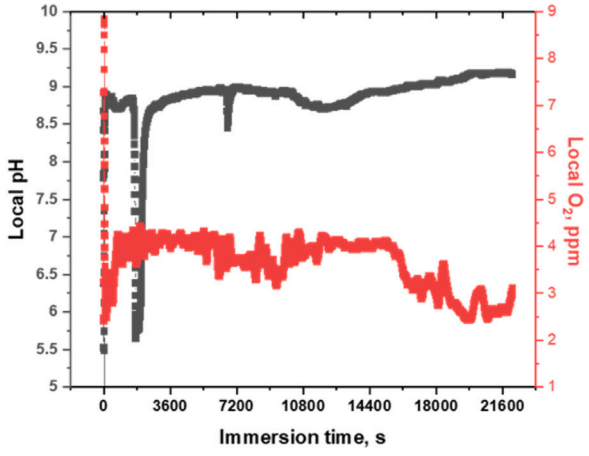

(b)

Fig. 10. SECM measurements of lithium carbonate corrosion inhibitor sample: simultaneous pH (in black, left Y axis) and O_2 concentration (in red, right Y axis) at a static point in the center of the coating defect on AA2024-T3 over 6 h. (a) and (b) are two independent measurements taken on two parallel samples.

3.2. FEM results

The results of the corrosion and corrosion protection prediction models are 2D concentration maps of each of the introduced species in Table 1 as well as current density, metal surface potential and electrolyte potential 2D maps. These comprehensive 2D concentration maps and associated variables contribute valuable insights into the dynamic behavior of the protective system, providing a nuanced understanding of the spatial distribution and interaction of key species within the modeled environment.

Fig. 6 provides a focused view of the region around the defect within the primer, serving as the area of primary interest. Figs. 6(a), 6(b) are the distribution of lithium carbonate pigment over the simulation domains at the 0 and 11 h. Throughout this exposure time, Li_2CO_3 is exclusively located in the primer and depletion occurs at the primer-electrolyte interface. Similar figures representing Li^+ at same time points in Fig. 6(c), 6(d) show an increase in Li^+ concentration in all solution domains in general and especially in the primer and the electrolyte, following the decrease in Li_2CO_3 in the topcoat. However, the main focus is on the change in Li^+ concentration in the defect area, which shows a concentration value of around $1 mol\ m^{-3}$ = 1 mM at 11 h. Fig. 7 shows that the average concentration of the sum of all aluminum ion species listed in Table 1 is reduced significantly in the lithium carbonate case, indicating a discernible reduction in aluminum oxidation. This could indicate the corrosion protection effect of Li^+.

3.3. Model validation with local micro-probe measurements

3.3.1. pH and concentration of O_2

SECM surface scans were done for the reference sample at 1, 1.5 and 4 h as seen in Fig. 8. The depletion of oxygen concentration could be noted over time across Fig. 8a, c and e with a range of 3.9 to 6.5 ppm at 1 h to substantially lower ppm values of 1 to 2.4 ppm at 4 h indicating that the corrosion kinetics at the alloy surface are higher than the rate of oxygen replenishing from the atmosphere. A cathodic area is observed in the upper part of the map, evident by the lower oxygen concentration compared to the rest of the map. A counter anodic area could be observed at the right bottom corner of the respective scan. This may indicate a pit initiation region [11,29]. The same could be observed from the pH maps where local pitting activity is indicated by the acidic red zones at early times of 1 h and 1.5 h in Fig. 8b, d, respectively, but these zones are re-passivated at later times leaving a more homogeneous pH of around 7 across the surface in Fig. 8f.

A second set of SECM measurements were done on the lithium carbonate sample to record surface maps at 30 min, 3 and 6 h, as well as, changes at the center of the defect over 6 h. From Fig. 9b and f it is evident that the dominant pH over time is basic with values exceeding 8. This is mainly due to the effect of the carbonate released from the lithium carbonate pigment [6,30]. This indicates that the partial leaching has already taken place for 30 min. A significant difference in the pH could be seen at 3 h in Fig. 9d as it tends more towards acidic values, particularly, in the top part of the scan. This may point out a local anodic zone where, OH^- which together with the anodically dissolved Al^{3+} form aluminum hydrolysis products leading to a localized acidic pH. This could further be proved by the oxygen concentration in Fig. 9c at the same location showing higher values compared to the rest of the map. Later scan points show a general increase of basicity, indicating repassivation of the alloy surface as the concentration of lithium-ion increases and begins the formation of LDH and its associated surface protection. Oxygen concentration shows a lower concentration at 30 min as seen in Fig. 9a compared to reference sample at 1 h in Fig. 8a. This indicates that the inhibition has not taken full effect on the alloy surface. However, the oxygen concentration range remains almost consistent throughout the following time steps, pointing out the existence of some level of corrosion protection. This is particularly significant as oxygen replenishment through the air-electrolyte interface is slower in the coated sample than in the reference sample due to the higher thickness of the water layer.

Two sets of measurements were conducted at the center of the scratch in Fig. 10a, b. The results show a more consistent pH over time, with values near 8.5 to 9. That is, with an exception to a small dip to pH 6.1 at 1 h in Fig. 10a and pH 5.5 at 30 min in Fig. 10b. This abrupt change could be related to meta(stable) pitting, as a local dissolution of aluminum followed by hydrolyzation results in a decrease in the local pH with values approaching 3.65 [31]. The pit's effect is not reflected in oxygen consumption, as the area of cathodic activity supporting

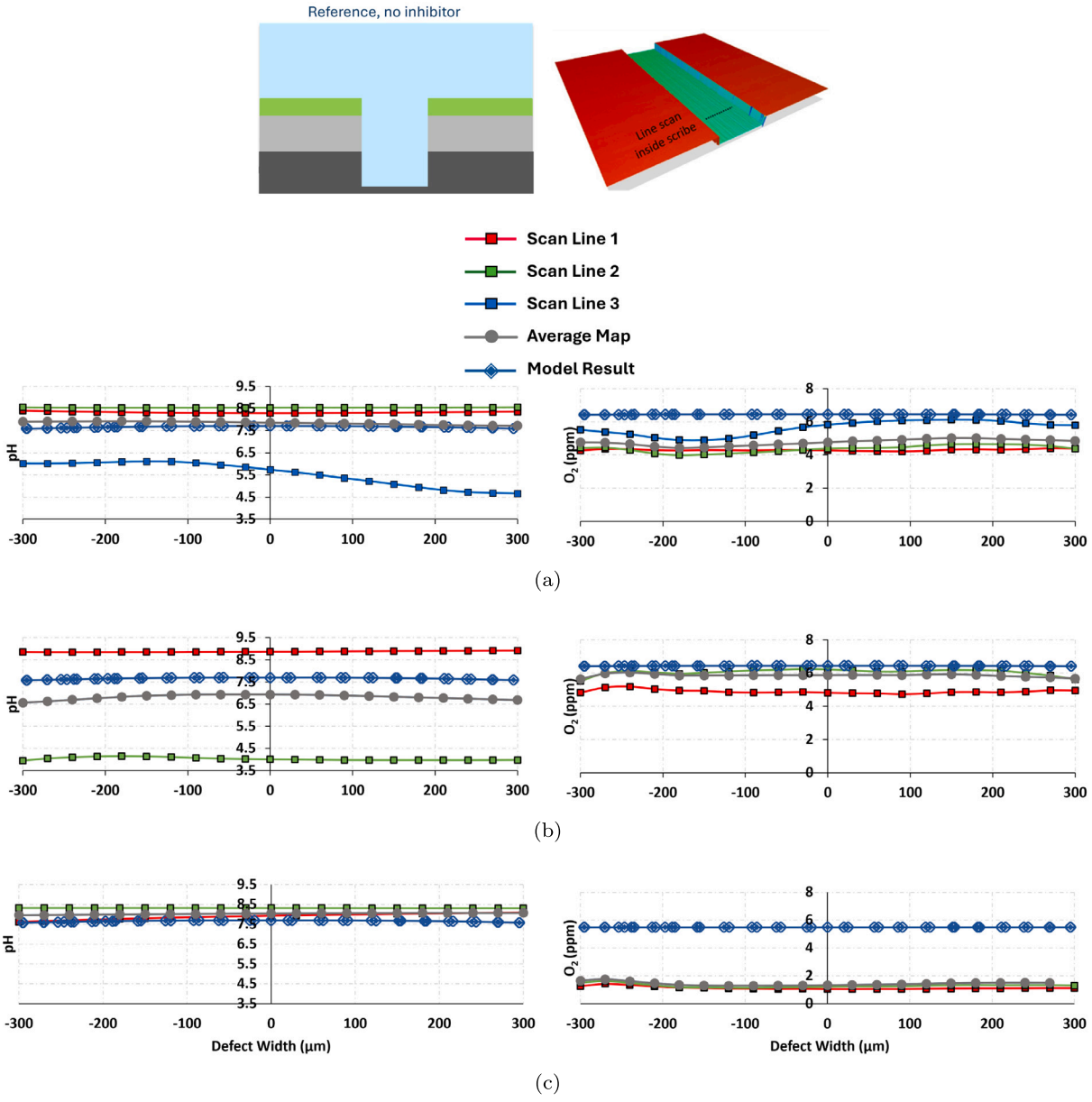

Fig. 11. Model results versus SECM measurements for the reference case: pH and O_2 concentration at three time points: (a) 1 h, (b) 1.5 h and (c) 4 h.

anodic activity is typically much larger and is not concentrated in a single point/pit. This corresponds to a similar overall pH decrease in the surface maps at the same time point in the top part of Fig. 9d. The value of pH is quickly restored to the basic zone, suggesting that it was indeed a formation of protective LDH causing the protective behavior as the pigment ions arrive at the zone is expected to cause a basic environment [27,28]. The oxygen concentration shows a more gradual decrease over time, but not as significant as what is seen in the surface map of the unprotected sample. While corrosion inhibition has indeed started, it has not yet reached its optimum state of 10.6 pH. This could be supported by examining the oxygen map for lithium carbonate inhibited sample at 6 h in Fig. 9g as it shows some high oxygen zones specially when compared to the reference sample at 4 h in Fig. 8g.

For comparison purposes, scan lines across the scribe width were extracted from the SECM maps in Figs. 8 and 9. The selected lines were extracted horizontally across the map (from the left side to the right side) specifically in regions where the changes are minimal in the horizontal direction. This is done to simplify the model comparison since the measurements are 2 dimensions across the surface of AA2024-T3 while the model is 2D perpendicular to the AA2024-T3 surface. It should be noted that as the alloy's surface is heterogeneous, different electrode reactions occur at different surface locations which results in a varying zones in the map as seen in Figs. 8, 9. This variation would still be observed in some of the line scans and would contradict with the model's assumption of a homogeneous surface. This necessitated the extraction of another line from the measurements representing the average values of the horizontal map, such that the measurement is representing a homogeneous distribution, which would make it closer to the model assumption of a homogeneous alloy surface.

Scan lines of pH, which could be calculated from the concentration of hydrogen ions and scan lines of oxygen, are extracted from the 2D model results at a height of 20 μm from the electrode surface to align with the location of measuring scanning probes. Fig. 11 shows a comparison between model results and experimental measurements in the uninhibited reference case. At 1 h, the model results show better agreement with the average map and most of the scan lines, while seems to slightly exceed the values of O_2 concentration compared

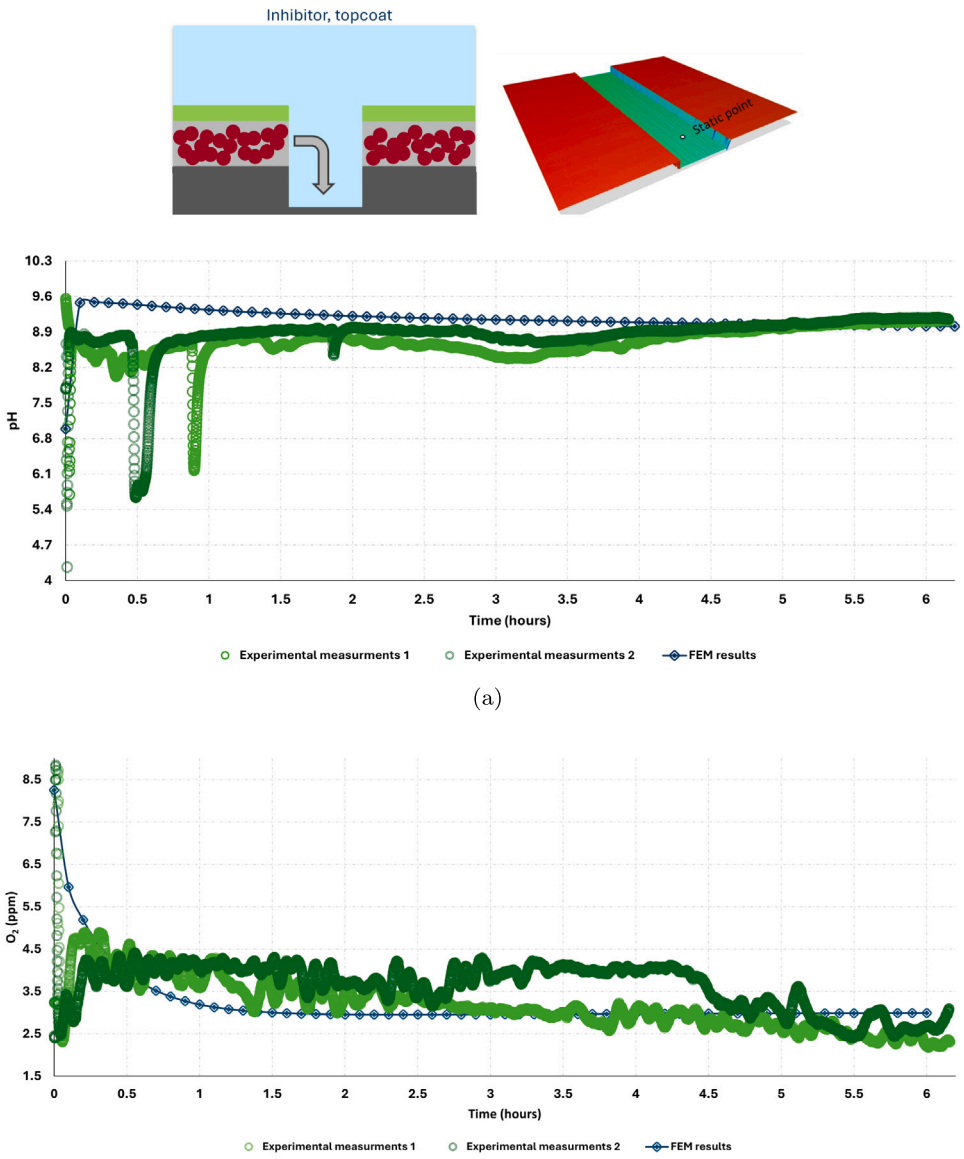

Fig. 12. Model results versus SECM measurement of the lithium carbonate corrosion inhibitor case for pH and O_2 concentration at the center of the coating defect over time. (a) pH values evolution over time, (b) dissolved Oxygen concentration values evolution over time.

to the measurement lines. At 1.5 h, the model predictions between the average and some scan lines for pH with a better prediction of oxygen concentration. At 4 h, pH predictions of the model lies close to the SIET results. However, the model oxygen concentration deviates significantly from all measurements, indicating that the model tends to replace the consumed oxygen at a higher rate than at the experimental measurements. A possible explanation could be the changing rate of oxygen replenishment in the experimental setup due to the changing thickness of the water layer over time. This is an effect that the model does not take into consideration: in the model, the water layer thickness along with the rate of oxygen dissolution into the electrolyte remain the same throughout the exposure time.

Examination of the lithium carbonate case results in Fig. 12 demonstrate the model's capability of predicting pH values over time. In general, the results for the corrosion protected case show good agreement with the experimental results, especially with the measurements at the defect center in Fig. 12. The predicted pH values at defect center approach the measured values for over 6 h, suggesting that the behavior of lithium carbonate and its resulting pH outcome is accurately represented in the model. That is, aside from the small pH dips in the measurements. The overall trend, beginning with the jump in pH value or the dip in oxygen concentration followed by a long steady state in both cases, could be seen clearly in the model results. The discrepancies observed in the pH graph of Fig. 10a at 1 h and Fig. 10b at 30 min between some of the scan lines and the model results but could be connected to the formation of a small local pit, which the model could not reproduce with a homogeneous surface assumption. A closer look at line scans across the sample compared to a line scan across the model geometry are presented in Fig. 13. At 30 min and 3 h, the model agrees with at least one of the measurement lines. A better alignment could be seen at 6 h for both pH and O_2 concentration.

3.3.2. Current density

In parallel with the SECM measurements, SVET measurements were conducted to record the distribution of current density in the coating defect to validate the predicted current density values in the FEM model. The SVET measurements were conducted over the entire defect area for the uninhibited reference sample and the Li_2CO_3 containing

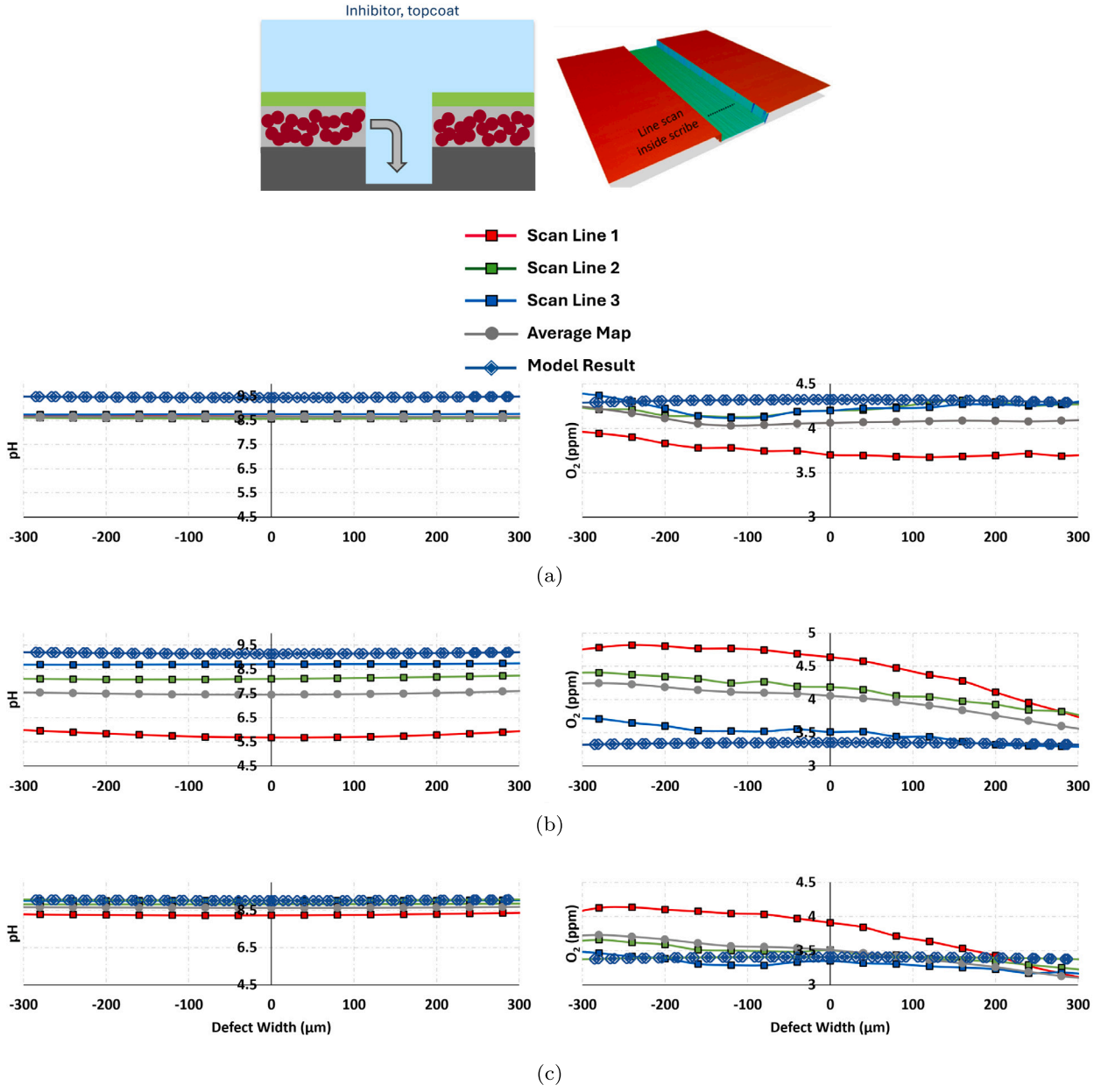

Fig. 13. Model results versus SECM measurement for lithium carbonate inhibited sample: pH and O_2 concentration at three time points: (a) 30 min, (b) 3 h and (c) 6 h.

sample, and comparable data for both after 6 h of immersion in the electrolyte are presented.

For the purpose of the model validation, the interest was directed towards the current density in the direction perpendicular to the defect surface J_z of the three experimentally measured current vector components (J_x, J_y and J_z). The results are shown in Fig. 14 where the red zones are pitting locations indicated by their positive anodic current values. It is noted that the lithium carbonate inhibited sample shows smaller number of pits, though no change is detected in the intensity of the remaining pits. This may indicate that some pits have already been repassivated by the effect of the protective LDH formation, while some areas continued to corrode without the inhibition playing an effect.

Since the model considers a homogeneous surface of AA2024-T3 where both oxidation and reduction reactions occur simultaneously over the entire alloy surface, it is impossible to obtain any local activities in the model. In contrast, local activity represented through pits occur in the measurements as seen in the highly anodic zones indicated by their red colors in Fig. 14 as previously discussed. To be able to successfully compare model predictions with SVET validation measurements, a representative active node is added to the model at the edge of the defect on the right as seen in Fig. 15, at the same location as a pit is visible in the SVET measurement. This concept aims to represent a transition of the homogeneous assumption into a simplified heterogeneous model, thereby reducing the limitations associated with the homogeneous approach. It should be noted that this active node does not represent only one pit but rather the overall ratio of active anodic surface to inactive surface. The active node is implemented to have a higher oxidation reaction rate compared to the rate in the remaining surface of the alloy [12,13]. The size, calculated from the area ratio, and the intensity factor are calculated from [32] which combined in situ EN measurements with optical measurements of a corroding AA2024-T3 surface conducted in the initial 400–600 s of immersion in the electrolyte to detect transient intense peaks representing pits initiation. The results of this work gave a ratio of the active surface area to total surface area, along with a ratio of the intensity of the active surface relative to the activity of the rest of the surface. Upon

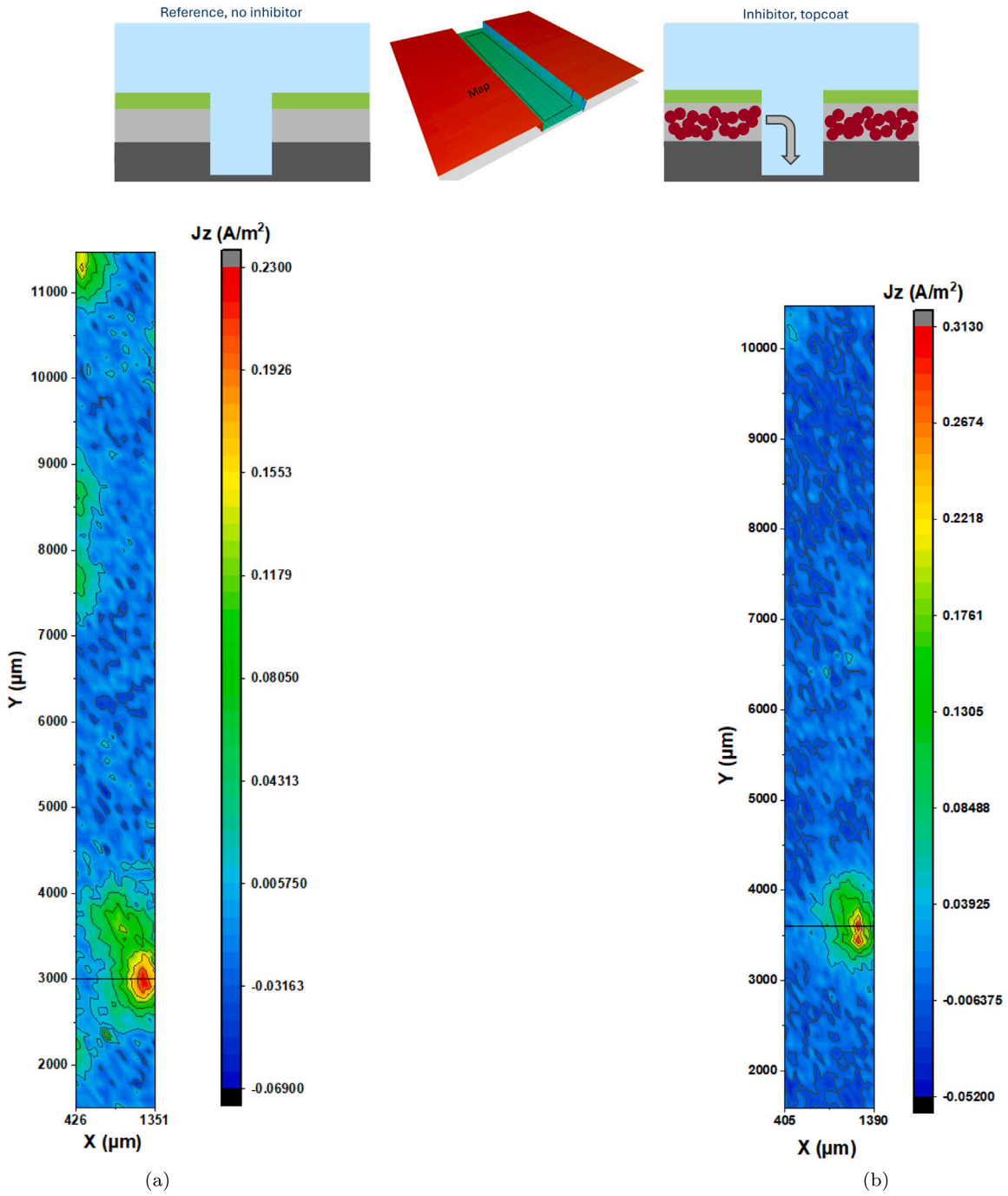

Fig. 14. SVET measurements of current density vector perpendicular to AA2024-T3 surface j_z. (a) Reference sample at 6 h, (b) lithium carbonate sample at 6 h.

utilizing this, it was possible to obtain these parameters for this model's particular active node which has a length of 0.375 µm and an intensity of 40 000. The current density component perpendicular to the alloy was extracted from the FEM and the active node model at 6 h at a height of 200 µm and compared to a line scan from the experimental measurements extracted from an area where a pit has been formed at a similar probe height of 200 µm.

Figs. 16, 17 show the results of the experimental SVET results compared to the FEM results of the homogeneous and the heterogeneous models. Fig. 16 shows the current distribution across scan lines. Both figures demonstrate the need for the active node model when it comes to calculating corrosion current densities. While Fig. 17 focuses on the overall maximum values of the anodic and cathodic currents obtained. The homogeneous model greatly underestimates the current values. This is expected as it disregards the main source of anodic activity, which is pitting due to the nature of the alloy [24]. A closer look at the results of the homogeneous model shows a variation in the anodic and cathodic activities across the defect width, with more anodic activity closer to the coating edges and more cathodic activity in the middle region. This variation is attributed to edge effects where the sharp right angle of the defect corners forces this region to be higher in potential, which affects the electrode and electrolyte current densities as a result. More importantly, both the heterogeneous model and the experimental scan line show a similar behavior with the current being highly anodic at the active node location as depicted in Figs. 15 and 14(a) and gradually shifts towards negative values until reaches a maximum value of cathodic current on the left side of the defect. The quantitative comparison in Fig. 17 shows close resemblance with

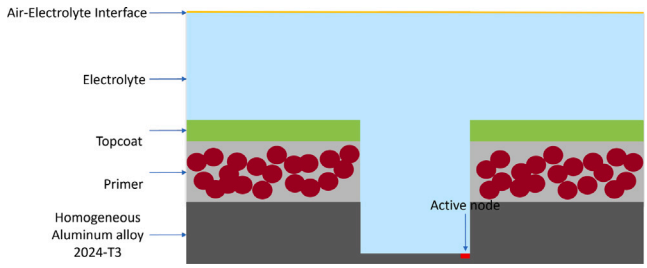

Fig. 15. Modified model geometry by introduction of an active node representing a local anodic node.

the measured anodic current density, with an overestimation of the cathodic current density. This may be attributed to the differences in capturing the results between experiments and numerical models. While experimental methods capture a part of the surface in the 2D scan with longer defect surface extending parallel to the coat, the model is a defined 2D geometry with no geometry extensions that may include any more data. This effect is particularly important in the case of current density as its distribution in a conductive media (electrode and electrolyte) would be hugely dependent on the entire surface considering that the total anodic and cathodic current densities across the surface would have to be equal seeing that the alloy surface is conductive and obeys charge conservation rules. A further evidence are the calculated sums of cathodic and anodic currents in SVET measurements in x, *y* and z: 0.198, −3.57 and 10.03 Am^{-2} for the area under investigation, showing values > 0.

Similarly, The heterogeneous active node is introduced in the lithium carbonate protected model. The multiple implement parts of the model posed a complexity that prevented the model from converging with the needed node activity factor, leading to model continuous failure. Removal of the topcoat domain from the model was implemented as a mitigation strategy that led to model convergence without further disruption of the nonlinear model. The results of the lithium carbonate case are in line with the reference case in many aspects. While the homogeneous model continues to underestimate the maximum anodic and cathodic current density values, the heterogeneous model manages to predict the anodic value and yet overestimates the cathodic value. Current density lines across the defect width for SVET measurements and FEM models are shown in Fig. 18. The values of the maximum anodic and cathodic currents of SVET measurements compared to the FEM homogeneous and heterogeneous models are shown in Fig. 19. The homogeneous model continues to be unable to predict the current densities, while the heterogeneous model demonstrates higher anodic behavior close to the active node. As the heterogeneous model scan line move to the left and away from the active node location, surface activity begins to shift towards a cathodic nature. On contrast, the SVET scan line remains anodic as it moves to the left, making comparison between the measurements and model difficult. Nonetheless, obtaining a different SVET scan line was not possible, as it was necessary for the line to pass through an anodic active area from Fig. 14.

3.4. A parametric study to predict the corrosion protection descriptors

Having the model successfully validated, it is extended to assess the effect of varying the width of the created defect in the coating and its consequent effect on Li^+ concentration and pH. Since these two factors play an important role in the protection process [6,8] and as such could be used as descriptors of the offered corrosion protection. Two study

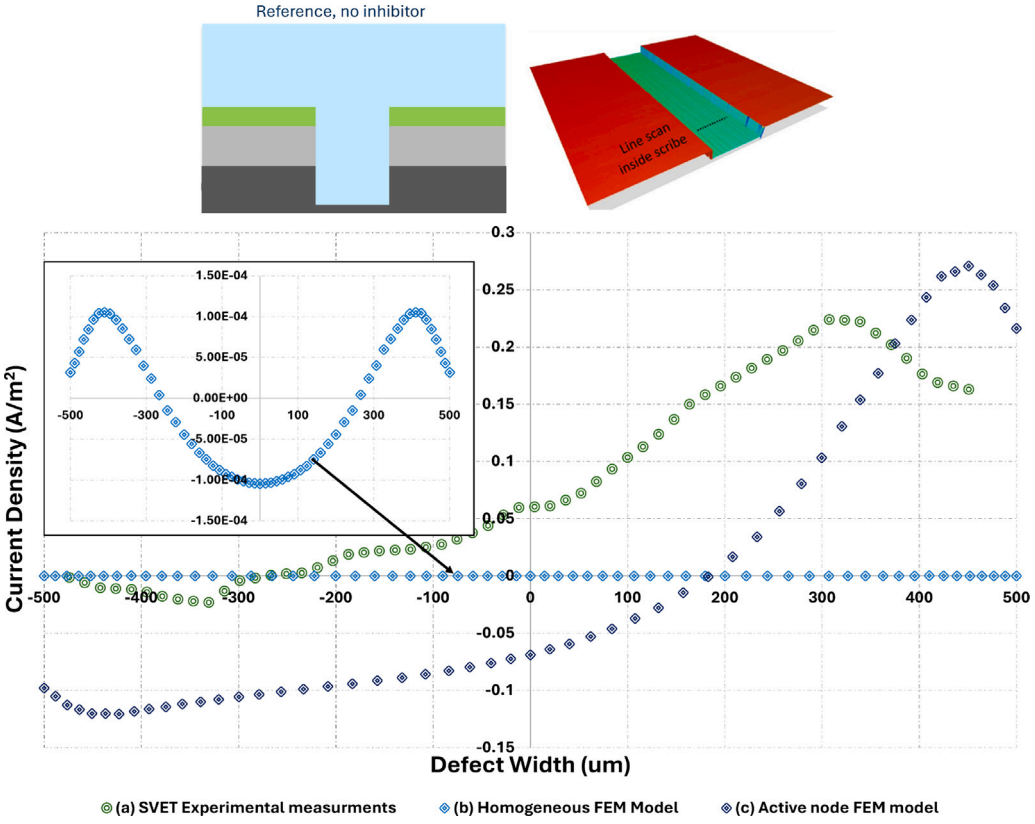

Fig. 16. Model results versus SVET measurements of uninhibited reference for current density at 6 h for the heterogeneous model containing the active node.

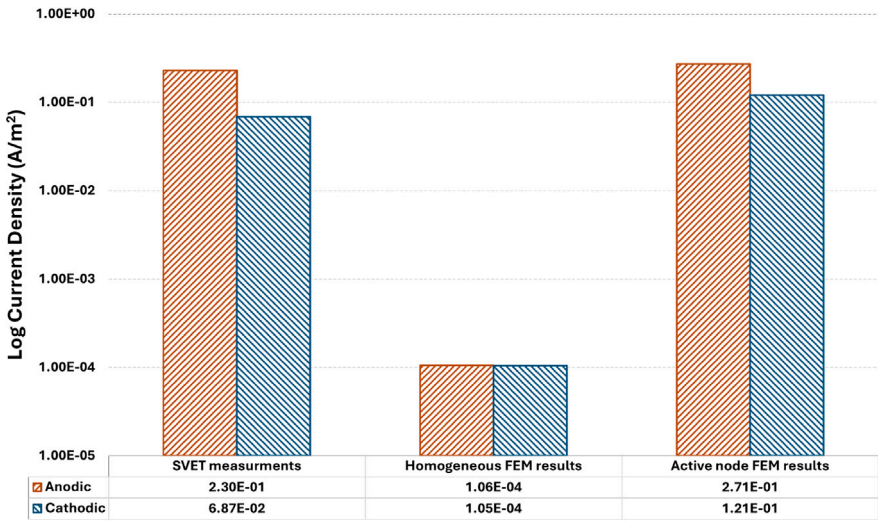

Fig. 17. Maximum anodic and cathodic current density values between measurements and the homogeneous and heterogeneous models for uninhibited reference case.

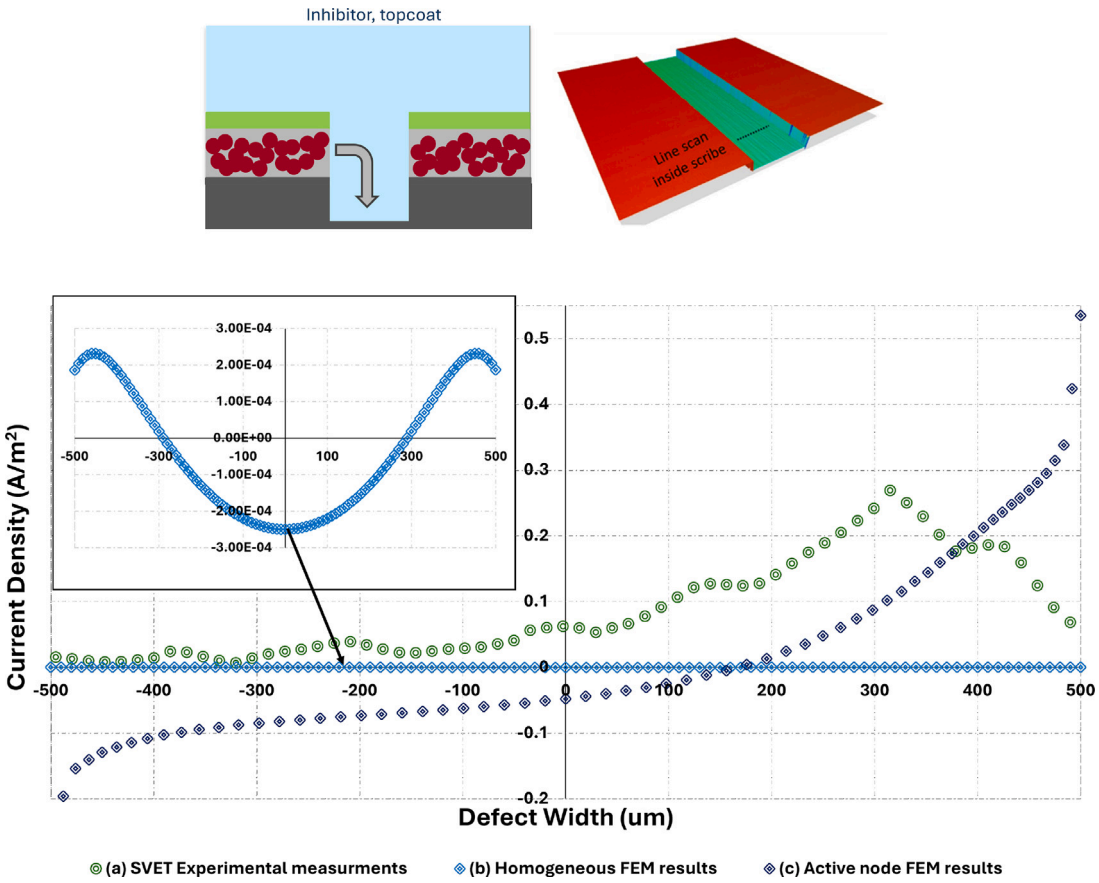

Fig. 18. Model results versus SVET measurements of lithium carbonate coated sample for current density at 6 h for the heterogeneous model containing the active node.

cases were chosen: the first considering different values of defect width, and the second employs multiple PVC values.

Defect width values equal to 0.2 μm, 0.5 μm, 0.8 μm and 1.1 μm were chosen to cover a wide range of possibilities of the created damage to the coating. The parametric study was conducted for 20 h of simulation time per parameter, with the results obtained at the center of the defect at the alloy surface are presented in Fig. 20. Fig. 20(a) shows the concentration of Li^+ over time in mol/m^3 on the left y-axis and in M on the right y-axis. It could be seen that the defect size plays a significant role in the concentration of Li^+ with the effect most observed at 0.2 μm. However, the defect size seems to play an insignificant role on the pH in the center of the defect, as presented in Fig. 20(b). The difference

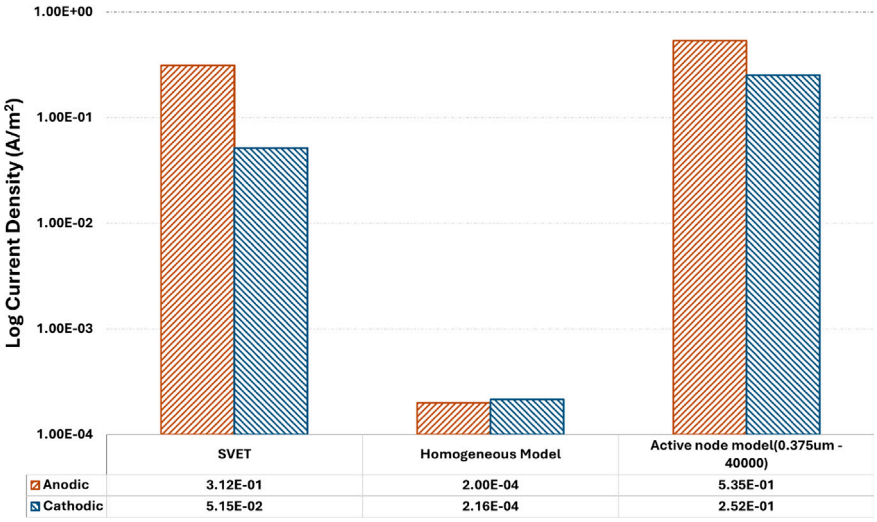

Fig. 19. Maximum anodic and cathodic current density values between measurements and the homogeneous and heterogeneous models of the lithium carbonate protected sample.

after 20 h is minor even between defect sizes of 0.2 μm and 1.1 μm. A common behavior across defect sizes is observed in the pH values as they initially make a considerable jump to basic values higher than 9 but then gradually decrease and plateau after five hours.

Similar to the first study, another study scanning initial PVC% values equal to 1.75%, 5.3%, 8.7%, 12.2%, 15.8% were conducted with the results obtained at the center of the defect and presented in Fig. 21. The variation in PVC values does not affect the general trend of the results over 20 h. It could be seen that the increase of the initial concentration of Li_2CO_3 affects pH and the concentration of Li+ at the center of the defect. The pH values initially make a considerable rise to basic values above 9 with small differences between the pH values across different PVCs. The plot lines gradually decrease and plateaus towards values less than 9 pH after the first hour.

4. Conclusion

A 2D finite element tertiary current distribution model is developed in Comsol Multiphysics to predict AA2024-T3 corrosion and corrosion inhibition by lithium carbonate particles loaded in a primer and topped with a topcoat. Two cases were examined: one involving a reference sample, coated with uninhibited primer-topcoat system, freely corroding AA2024-T3 surface with a defect introduced into the coating, and another considering corrosion protection achieved by dissolution and leaching of lithium carbonate from the primer while maintaining the topcoat nearly devoid of inhibitor species. In both cases, the model accounted for electrode reactions at the metal surface, and reactions involving metal hydrolysis, inhibitor dissolution, and further interactions with dissolved species in the electrolyte. Additionally, the model considered diffusion and leaching of all species across the defined domain in the system: primer, topcoat and electrolyte. This comprehensive approach aimed to capture the intricate dynamics associated with both corrosion and corrosion protection scenarios. Two distinct experimental measurements were used as inputs; potentiodynamic polarization of AA2024-T3 in 0.1 M sodium chloride combined with varying concentration of lithium carbonate and leaching measurements from a coating loaded with lithium carbonate with an artificial defect extending to the underlying AA2024-T3 substrate. The input measurements underwent processing and fitting to derive two sets of numerical values. The first set established the relationship between lithium carbonate concentration and the activity level of AA2024-T3 redox reactions, while the second set characterized the temporal evolution of Li^+ concentration in the defect. Model results include the 2D concentration changes of all involved species over an 11-h simulation period, as well as, electrode current density and electrode potential. The reliability of the formulated model is assessed by model validation using a third set of experimental data obtained through electrochemical microscopy (SECM) in potentiometric and amperometric mode and scanning vibrating electrode technique (SVET) in terms of the pH, O_2 concentration and current density, respectively. The validation showed the following:

- Oxygen concentration and pH were compared with model output, revealing a notable agreement, particularly at later time points. Earlier time points suggest that the model tends to progress in values more rapidly compared to the measurements. Small variations were identified in O_2 concentration between model results and measurements. They are explained with the local effects occurring on the heterogeneous surface of AA2024-T3. It is important to note that these variations, being stochastic in nature, could not be accurately represented by the model, which assumes a homogeneous surface for the aluminum alloy.
- Though the model has successfully predicted oxygen concentration and pH, its homogeneous assumption posed an obstacle for current density prediction. Current density measurements were compared to two versions of the model, one with a homogenized surface of AA2024-T3 and another with an introduced active node to the surface to resemble local corrosion. While the introduction of an active node has proven sufficient to approach the measured values of current densities and established the model's capability to expand and engulf the heterogeneity of AA2024-T3 surface, it pointed out the necessity of taking into consideration pits activity when calculating current density in particular.

This model holds the potential for extension to consider other inhibitor pigments, as long as, the input values are adjusted to represent the characteristics of the new system. This extension enables the prediction of the optimum concentration of effective inhibitors to obtain enhanced surface protection, while giving an insight into the required time to reach this protection level.

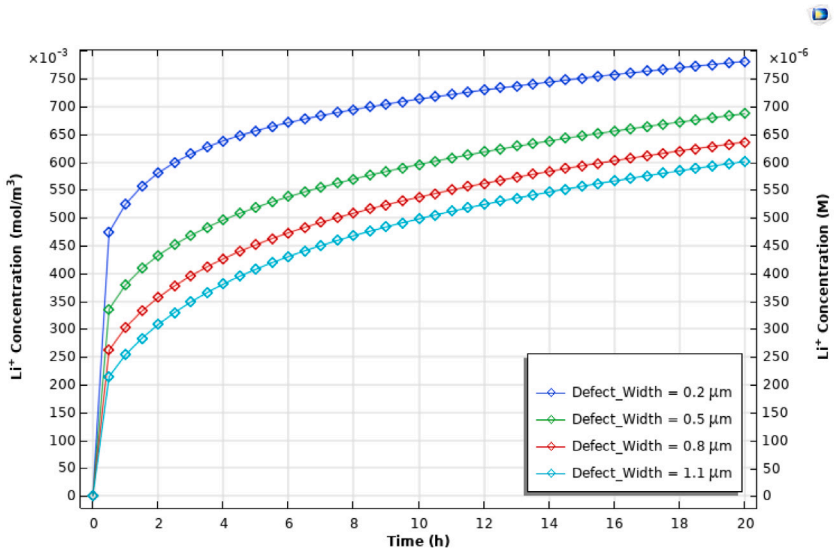

(a)

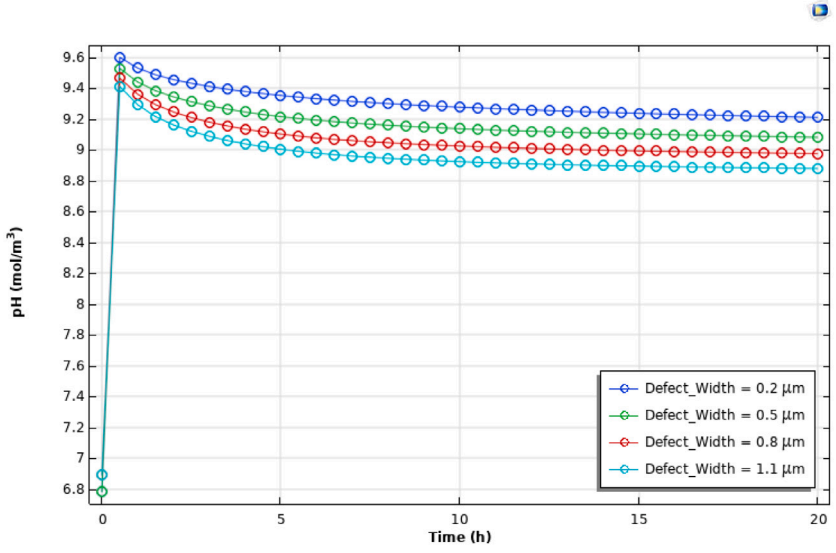

(b)

Fig. 20. A relation between the effect of the width of the defect introduced to the coating layer on the concentrations of Li^+ and the resulting pH, in order to predict protection. (a) Change in Li^+ concentration over time, (b) change in pH values over time.

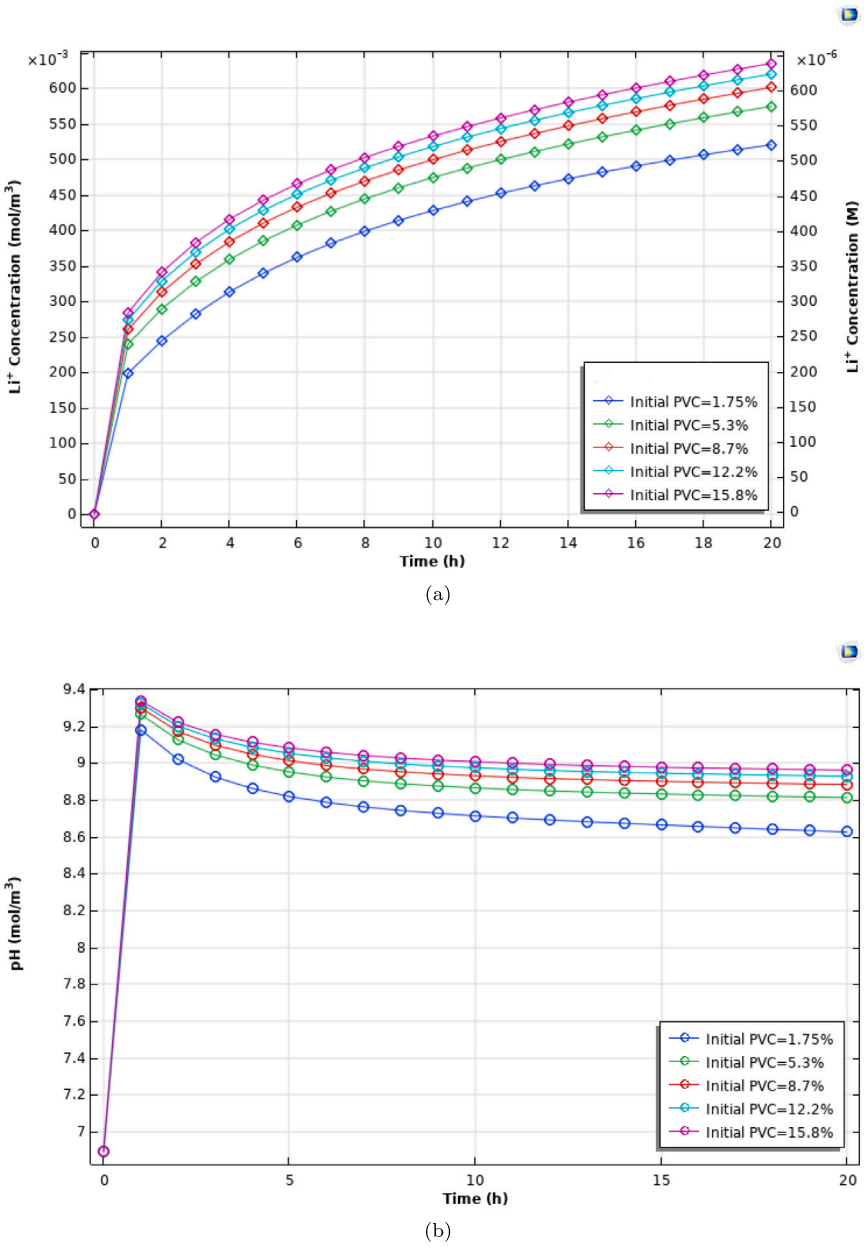

Fig. 21. A relation between the effect of initial Li_2CO_3 corrosion inhibitor PVC in the primer on the concentrations of Li^+ and the resulting pH, in order to predict protection. (a) Change in Li^+ concentration over time, (b) change in pH values over time.

CRediT authorship contribution statement

N. Abdelrahman: Writing – review & editing, Writing – original draft, Visualization, Methodology, Formal analysis, Conceptualization. **N. Van den Steen:** Methodology, Conceptualization. **C. Özkan:** Writing – review & editing, Data curation. **C. Wang:** Validation, Data curation. **C. Song:** Validation, Data curation. **P. Visser:** Writing – review & editing, Data curation, Conceptualization. **S.V. Lamaka:** Writing – review & editing, Validation, Supervision, Data curation, Conceptualization. **S. Kallip:** Writing – review & editing, Data curation. **R. Böttcher:** Writing – review & editing, Methodology. **J.M.C. Mol:** Writing – review & editing, Supervision, Conceptualization. **M.L. Zheludkevich:** Writing – review & editing, Visualization, Formal analysis, Conceptualization. **H. Terryn:** Writing – review & editing, Writing – original draft, Supervision, Methodology, Formal analysis, Conceptualization. **T. Hauffman:** Writing – original draft, Supervision, Methodology. **M. Meeusen:** Writing – review & editing, Writing – original draft, Supervision, Methodology, Formal analysis, Conceptualization.

Declaration of competing interest

The authors declare the following financial interests/personal relationships which may be considered as potential competing interests: Nourhan Abdelrahman reports financial support were provided by Horizon 2020 European Innovation Council Fast Track to Innovation. If there are other authors, they declare that they have no known competing financial interests or personal relationships that could have appeared to influence the work reported in this paper.

Acknowledgments

- This research is funded by Horizon2020 in the frame of VIPCOAT project H2020-NMBP-TO-IND-2020, Grant Agreement 952903.
- The authors wish to acknowledge the support of Elsyca NV throughout the steps of this work.
- The resources and services used in this work were provided by the VSC (Flemish Supercomputer Center), funded by the Research Foundation — Flanders (FWO), Belgium and the Flemish Government.

Appendix A. Supplementary data

Supplementary material related to this article can be found online at https://doi.org/10.1016/j.corsci.2025.112861.

Data availability

Data will be made available on request.

References

[1] M. Kendig, et al., Role of hexavalent chromium in the inhibition of corrosion of aluminum alloys, Surf. Coat. Technol. 140 (1) (2001) 58–66.
[2] Vic Armstrong, et al., Overview of REACH: Issues involved in the registration of metals, Neurotoxicology 83 (2021) 186–198.
[3] M.W. Kendig, R.G. Buchheit, Corrosion inhibition of aluminum and aluminum alloys by soluble chromates, chromate coatings, and chromate-free coatings, Corrosion 59 (5) (2003) 379–400.
[4] Sviatlana V. Lamaka, et al., High effective organic corrosion inhibitors for 2024 aluminium alloy, Electrochim. Acta 52 (25) (2007) 7231–7247.
[5] Peter Visser, Herman Terryn, Johannes MC. Mol, Active corrosion protection of various aluminium alloys by lithium-leaching coatings, Surf. Interface Anal. 51 (12) (2019) 1276–1287.
[6] Kristof Marcoen, et al., Compositional study of a corrosion protective layer formed by leachable lithium salts in a coating defect on AA2024-T3 aluminium alloys, Prog. Org. Coat. 119 (2018) 65–75.
[7] J.S. Laird, et al., Li leaching from Lithium Carbonate-primer: An emerging perspective of transport pathway development, Prog. Org. Coat. 134 (2019) 103–118.
[8] E. Michailidou, et al., The effect of pH on the corrosion protection of aluminum alloys in lithium-carbonate-containing NaCl solutions, Corros. Sci. 210 (2023) 110851.
[9] P. Visser, et al., The chemical throwing power of lithium-based inhibitors from organic coatings on AA2024-T3, Corros. Sci. 150 (2019) 194–206.
[10] Olga Guseva, et al., Modelling of anodic dissolution of pure aluminium in sodium chloride, Electrochim. Acta 54 (19) (2009) 4514–4524.
[11] Levente-Csaba Abodi, et al., Modeling localized aluminum alloy corrosion in chloride solutions under non-equilibrium conditions: steps toward understanding pitting initiation, Electrochim. Acta 63 (2012) 169–178.
[12] Olga Dolgikh, et al., Corrosion protection of steel cut-edges by hot-dip galvanized Al (Zn, Mg) coatings in 1 wt.
[13] Darya Snihirova, et al., Galvanic corrosion of Ti6Al4V-AA2024 joints in aircraft environment: Modelling and experimental validation, Corros. Sci. 157 (2019) 70–78.
[14] C. Vicente Moraes, et al., Finite element modeling of chemical and electrochemical protection mechanisms offered by Mg-based organic coatings to AA2024-T351, J. Electrochem. Soc. 168 (5) (2021) 051505.
[15] E. Javierre, et al., Tailoring the release of encapsulated corrosion inhibitors from damaged coatings: controlled release kinetics by overlapping diffusion fronts, Prog. Org. Coat. 75 (1–2) (2012) 20–27.
[16] Paul J. Denissen, Axel M. Homborg, Santiago J. Garcia, Requirements for corrosion inhibitor release from damaged primers for stable protection: A simulation and experimental approach using cerium loaded carriers, Surf. Coat. Technol. 430 (2022) 127966.
[17] Bart Van Den Bossche, Johan Deconinck, Gert Floridor, Pirode manual v. 2 (1), 2003.
[18] P. Visser, et al., Li leaching from Li carbonate-primer: Transport pathway development from the scribe edge of a primer/topcoat system, Prog. Org. Coat. 158 (2021) 106284.
[19] O. Dolgikh, A.S. Demeter, S.V. Lamaka, M. Taryba, A.C. Bastos, M.C. Quevedo, J. Deconinck, Simulation of the role of vibration on Scanning Vibrating Electrode Technique measurements close to a disc in plane, Electrochim. Acta 203 (2016) 379–387.
[20] A.C. Bastos, M.C. Quevedo, M.G.S. Ferreira, The influence of vibration and probe movement on SVET measurements, Corros. Sci. 92 (2015) 309–314.
[21] A.C. Bastos, M.C. Quevedo, O.V. Karavai, M.G.S. Ferreira, Review—On the application of the scanning vibrating electrode technique (SVET) to corrosion research, J. Electrochem. Soc. 164 (2017) C973–C990.
[22] John Rumble (Ed.), CRC handbook of chemistry and physics, 2017.
[23] Alan L. Soli, Robert H. Byrne, CO2 system hydration and dehydration kinetics and the equilibrium CO2/H2CO3 ratio in aqueous NaCl solution, Mar. Chem. 78 (2-3) (2002) 65–73.
[24] A.E.H.A. Boag, et al., How complex is the microstructure of AA2024-T3? Corros. Sci. 51 (8) (2009) 1565–1568.
[25] Zoi Manoli, et al., Transport of Electrolyte in Organic Coatings on Metal, in: Paint and Coatings Industry, IntechOpen, 2018, pp. 87–114.
[26] Wei Zhang, Dongshuai Hou, Hongyan Ma, Multi-scale study water and ions transport in the cement-based materials: from molecular dynamics to random walk, Microporous Mesoporous Mater. 325 (2021) 111330.
[27] Peter Visser, et al., Mechanism of passive layer formation on AA2024-T3 from alkaline lithium carbonate solutions in the presence of sodium chloride, J. Electrochem. Soc. 165 (2) (2018) C60.
[28] Peter Visser, et al., The corrosion protection of AA2024-T3 aluminium alloy by leaching of lithium-containing salts from organic coatings, Faraday Discuss. 180 (2015) 511–526.
[29] Levente-Csaba Abodi, Simulation of electrochemical processes on a micro-scale applied to aluminium corrosion, 2014.
[30] J.C.S. Fernandes, M.G.S. Ferreira, Effect of carbonate and lithium ions on the corrosion performance of pure aluminium, Electrochim. Acta 37 (14) (1992) 2659–2661.
[31] D. Snihirova, S.V. Lamaka, M. Taryba, A.N. Salak, S. Kallip, M.L. Zheludkevich, M.G.S. Ferreira, M.F. Motemor, Hydroxyapatite microparticles as feedback-active reservoirs of corrosion inhibitors, Acs Appl. Mater. Interfaces 2 (2010) 3011–3022.
[32] Paul J. Denissen., Axel M. Homborg, Santiago J. Garcia, Interpreting electrochemical noise and monitoring local corrosion by means of highly resolved spatiotemporal real-time optics, J. Electrochem. Soc. 166 (11) (2019) C3275.